AN EXPERIMENTAL INVESTIGATION OF THE FOREBODY OF A HYPERSONIC INLET MODEL AND A COMPARISON WITH THEORY

By

Carl Arthur Trexler

Thesis submitted to the Graduate Faculty of the
Virginia Polytechnic Institute and State University
in candidacy for the degree of

MASTER OF SCIENCE

in

Mechanical Engineering

April 1971

AN EXPERIMENTAL INVESTIGATION OF THE FOREBODY OF A HYPERSONIC INLET MODEL AND A COMPARISON WITH THEORY

by

Carl Arthur Trexler

Thesis submitted to the Graduate Faculty of the
Virginia Polytechnic Institute and State University
in partial fulfillment of the requirements for the degree of

MASTER OF SCIENCE

in

Mechanical Engineering

APPROVED:

Chairman, Dr. Robert A. Comparin

Dr. J. R. Mahan

Dr. Eugene F. Brown

April 1971

Blacksburg, Virginia

ACKNOWLEDGMENTS

The author wishes to express thanks to the National Aeronautics and Space Administration for the use of research facilities at the Langley Research Center in acquiring the data presented in this thesis. Appreciation is also expressed to Dr. Robert A. Comparin and Dr. Eugene F. Brown of the Virginia Polytechnic Institute and State University for their advice and their assistance in organizing the data. A special thanks to Mrs. Ann Simmonds for her aid in the preparation of the figures, and to his wife, Jimette, and Mrs. Carole Batterson for typing drafts of the text. The author would also like to thank Mrs. Pat Reagon for proofreading the text and the figures.

TABLE OF CONTENTS

LIST OF FIGURES

LIST OF SYMBOLS

h	enthalpy
l	probe length (see fig. 5), centimeters
L	model length (see fig. 4), centimeters
M	Mach number
p	static pressure
P_p	pitot pressure
R	gas constant
s	distance on compression surface parallel to plane of symmetry (see fig. 4), centimeters
T	temperature
u	velocity
W	model half-width (see fig. 4), centimeters
x,y,z	rectangular Cartesian coordinates (see figs. 3, 6, and 8)
α	sweep angle (see fig. 6), degrees
α_{max}	maximum sweep angle
β	ridge angle (see fig. 6), degrees
γ	ratio of specific heats
δ	flow deflection across shock wave, degrees
ϵ	shock wave angle, degrees
ϵ_c	shock wave angle measured on compression surface (see fig. 8)
λ	cross-flow angle (see fig. 6), degrees
ρ	density

ϕ	dihedral angle (see fig. 19), degrees
ψ	dihedral parameter, $\overline{DE}/\overline{AD}$ (see fig. 19)
ω	shock wave angle measured in xz plane (see fig. 6), degrees

Subscripts

1	free-stream conditions or the station in front of an oblique shock wave
2	conditions behind model shock wave (see fig. 8) or the station behind an oblique shock wave
3	conditions in model center region (see fig. 8)
n	components normal to oblique shock wave
N	components normal to compression surface leading edge
t	components tangential to oblique shock wave
τ	components parallel to compression surface leading edge

CHAPTER I

INTRODUCTION

While rocket propulsion systems are more completely developed than air-breathing systems for hypersonic flight, air-breathing systems have specific impulse characteristics which can be used to advantage in long-range suborbital missions as well as in the first stage of space shuttle flights (1)*. Several projects of the National Aeronautics and Space Administration have been concerned with the design and development of an air-breathing research engine capable of operation at Mach numbers from 4 to 8 (2). Another investigation by NASA deals with the first stage of a reusable space shuttle vehicle capable of reaching a flight Mach number of 12 (3). The proposed supersonic combustion ramjet engine for this system would have three-dimensional inlet modules attached to the bottom side of the fuselage. This arrangement permits the inlets to lie behind the vehicle shock wave utilizing the forebody to obtain external compression.

In order to fully develop the engine's capabilities, it has been necessary to carry out research projects on hypersonic inlets. Most inlets to date (4) suffer from the requirements of a large amount of variable geometry. There must be enough contraction at hypersonic speeds and enough spillage for starting at low Mach numbers. Several

*Numbers in parentheses refer to similarly numbered items in reference section.

attempts have been made to overcome this problem utilizing fixed geometry, swept-wedge compression surfaces, and side walls open back to the minimum area (5-6). An investigation of the flow field of such an inlet is the subject of this thesis.

Shown in figure 1 are four three-dimensional inlet modules attached to the undersurface of a hypersonic vehicle and lying within the flow field of the vehicle forebody. The inlet modules have planar surfaces, and the shock wave produced by the vehicle strikes the cowl lip at some design Mach number. Sweeping the cowl rearward and still catching the shock wave provides full capture during hypersonic flight and permits flow spillage for fixed geometry starting at low Mach numbers. Another benefit of the swept-wedge compression surface is the sharp leading edge presented to the approaching flow which tends to minimize drag and produces a large normal wedge angle. This large normal wedge angle provides for high heat-transfer rates, which reduce leading-edge cooling and construction problems. There is also the possibility of utilizing three-dimensional combustion characteristics (thermal compression) to increase the aerodynamic contraction ratio for efficient hypersonic operation.

The present investigation was made to experimentally determine the characteristics of supersonic flow over the initial compression surfaces of a swept-wedge inlet. A theoretical analysis for a simplified wedge flow model, which produces a flow field similar to that found in the experimental model, is introduced.

The experimental model's leading edge had a sweep angle of 55°, and the compression surface was oriented to provide (in the vertical plane) 8° of deflection to the Mach 4.0 flow (see fig. 2). The cowl, which would have been attached to the top of the model, was omitted. Tests were conducted in a 23-centimeter-square continuous-flow tunnel test section. The stagnation temperature was 300° K and the stagnation pressure was 13.6 atmospheres, giving a Reynolds number of 6.6×10^{7} per meter. Static pressures, pitot pressures, schlieren photographs, and oil streaks were obtained to determine the model's performance.

In the theoretical analysis, the working fluid was assumed to be a perfect gas having specific heat ratio of 1.4. The free-stream flow was broken into components and two-dimensional techniques were used to predict flow direction, Mach number, and shock wave structure. An appendix is included which contains a parametric study of swept-wedge compression surfaces and determines the limitations of the theoretical analysis.

CHAPTER II

EXPERIMENTAL MODEL AND FACILITY

The experiment was conducted at the Langley Research Center of the National Aeronautics and Space Administration located in Hampton, Virginia.

Test Apparatus and Model

A sketch of the swept-wedge model mounted in a square channel is shown in figure 3. Machine screws fastened the sides to the compression surface of the machined aluminum model. Thin films of room-temperature vulcanizing rubber were used as gaskets to prevent flow leakage between the sections. Two 1.27-centimeter-square steel rails were bolted to the model under side and they, in turn, were bolted to a flat plate spanning the square channel. This arrangement placed the model's 55° swept leading edges above the plate boundary layer and allowed the compression surface to present a true 8° ridge angle to the free stream. Sides or plows were provided to fill the region left by the flow turned inward by the swept leading edges.

A 39.0-centimeter-diameter duct continuously supplied the 23.0-centimeter-square test section through a two-dimensional nozzle. The test section exhausted through a throat and subsonic diffuser to the atmosphere. The average Mach number in front of the leading edges was 4.03, as obtained from previous calibration with the flat plate (7), and the stagnation pressure was 13.6 atmospheres, yielding a free-stream static pressure of 0.87 newton/centimeter^2. A test section

Reynolds number of approximately 6.6×10^7 per meter was calculated from these conditions and the ambient stagnation temperature (8). Channel mass flow was 15.5 kilograms/second.

Instrumentation

Tunnel stagnation pressure was measured by a U.S. 0-172 newton/centimeter^2 absolute gauge. The stagnation probe was located just upstream of the nozzle throat in the 39.0-centimeter-diameter duct.

Figure 4 shows the location of the 30 static pressure taps on the compression surface, which is presented in the figure parallel to the plane of the paper. Therefore, both sections of the compression surface are shown in a normal projection. Each pressure tap had a 0.152-centimeter OD, 0.102-centimeter ID, continuous monel tube cemented in plastic and finished flush with the compression surface. Static pressures were recorded on strip charts with automatic balance potentiometers attached to 6.9 newton/centimeter^2 differential pressure transducers. The three pressure transducers were connected to 12-port Scanivalves which provided for a maximum of 36 pressure readings. A reference pressure of -8.3 newtons/centimeter^2 gauge was applied to the back sides of the transducers with a vacuum pump to enable the gauges to read less than -6.9 newtons/centimeter^2 gauge. This pressure was controlled by a manostat and monitored with a mercury column.

Pitot probe survey stations over the compression surface are also shown in figure 4. Each station is identified by s, the distance from the fork formed by the intersection of the leading edges and the probe tips, measured down the center of the compression surface. The

pitot probe was a tube aligned approximately parallel to the flow, with the open end facing upstream (9). Therefore, the measured pitot pressure was the stagnation pressure behind the normal shock wave lying ahead of the probe.

Pitot probes of different lengths (see fig. 5) surveyed the flow field via two test section access locations. Surveys were made vertically by translating the probe shaft and laterally by yawing the probes. The probes were positioned with an electrically driven actuator and located with a potentiometer system. The probes were angled down at 8° to be more nearly parallel with the flow coming up the compression surface.

Probe number 3 tip was made smaller than probe number 2 tip to more precisely locate the shock waves, although a time lag was anticipated with the smaller tip. Pitot probe tip number 4 was flattened to record the pressure gradient close to the compression surface. The pitot pressure was also recorded on a strip chart utilizing a 17.2 newton/centimeter^2 differential pressure transducer and an automatic balance potentiometer.

Flow Visualization Techniques

Schlieren photographs were taken to locate the position of any shock waves above the model sides. A single-pass schlieren system consisting of a mercury vapor lamp, two parabolic mirrors, and a silvered horizontal knife edge permitted density variations in the test section to be photographed.

Oil-streak tests to determine the surface flow direction were conducted by placing small drops of blackened oil on the model surface. The droplets were placed in row patterns back from the leading edges. Supersonic flow was established in the test section as quickly as possible (approximately 6 seconds) and operation was sustained for 10 to 20 seconds. The model was then removed from the tunnel and photographed.

Data Reduction and Accuracy

The raw static and pitot pressure data were reduced and nondimensionalized by the free-stream static pressure. Static pressures were plotted as functions of distance along and across the compression surface to determine the effect of distance from the leading edges. Distances measured on the surfaces were nondimensionalized with either the model's partial length, L, or the distance of the pitot probe from the fork, s. Although the model was symmetrical, static pressure taps were located on both sides to determine flow misalignment. A total of 16 vertical and 3 horizontal pitot pressure surveys were made with the 4 pitot probes to determine the shock wave structure and to compare the experimental data with the analysis.

The pitot probes were yawed up to 10° without significant loss in the accuracy of the pressure measurements (10). At higher yaw angles, the pitot pressure would begin to decrease, but it was still possible to estimate the location of the shock waves if the amount of probe deflection could be determined. In one case the value of the pitot

pressure for probe number 2 was extended to the surface static pressure, and the probe tip vertical deflection was found to be less than approximately two probe tip diameters. With the same wind loading assumed for the smaller probe tip number 3, the probe was unable to more accurately locate shock waves. Because of the length of probe number 4, deflections were difficult to estimate and, consequently, data are presented only for the case of zero yaw. It was calculated that for maximum yaw the value of s increased two probe tip diameters for probe number 1 and three probe tip diameters for probe numbers 2 and 3.

CHAPTER III

THEORETICAL MODEL

To understand the model design and the flow field on the compression surface, it was necessary to study the mechanism which produces the shock wave generated by the swept leading edges. The problem can be approximated by a wedge with a swept leading edge when only half of the model is considered. This swept-wedge analysis indicated the need for the plows (sidewalls) to fill the region left by the cross-flow and suggested a region of complex flow near the center of the model. Before the results were obtained, a method was developed which calculated the flow across an oblique shock wave.

Shock Wave Calculation

A closed-form solution of the cubic equation of reference 8, dealing with oblique shock waves, is available in reference 11. However, the familiar oblique shock wave equations of references 12 and 13, but requiring an iterative solution, were used in this analysis as this method was more convenient.

A computer program for the CDC 6000 computer at the Langley Research Center was written to compute the flow properties behind the shock wave of a swept wedge. To obtain the governing equations, the continuity, momentum, and energy equations were combined with a state equation to give two independent equations for the static pressure rise across a shock wave. The aforementioned equations are:

$$\text{continuity} \quad - \quad \rho_1 u_1 = \rho_2 u_2 \tag{1}$$

$$\text{momentum} \quad - \quad p_1 + \rho_1 u_1^2 = p_2 + \rho_2 u_2^2 \tag{2}$$

$$\text{energy} \quad - \quad \frac{1}{2} u_1^2 + h_1 = \frac{1}{2} u_2^2 + h_2 \tag{3}$$

$$\text{state} \quad - \quad p = \rho RT \tag{4}$$

The continuity, momentum, and state equations are combined to give the first equation

$$\frac{p_2}{p_1} = 1 + \gamma M_1^2 \left(1 - \frac{\rho_1}{\rho_2}\right) \sin^2 \epsilon \tag{5}$$

where γ is the specific heat ratio, M_1 is the upstream Mach number, ρ_1/ρ_2 is the density ratio across the shock wave, and ϵ is the oblique shock angle. The second equation, obtained by combining the continuity, momentum, and energy equations to give one of the Rankine-Hugoniot relations, becomes

$$\frac{p_2}{p_1} = \frac{\dfrac{\gamma + 1}{\gamma - 1} \dfrac{\rho_2}{\rho_1} - 1}{\dfrac{\gamma + 1}{\gamma - 1} - \dfrac{\rho_2}{\rho_1}} \tag{6}$$

The final equation needed is one which relates the density ratio, ρ_2/ρ_1, back to the shock angle, ϵ, and the flow turning angle, δ. From the diagram of an oblique shock wave

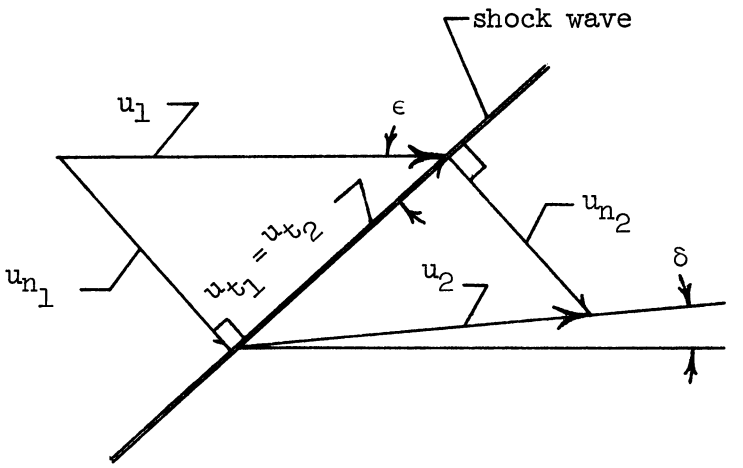

the normal velocity component, u_{n_1}, crosses a normal shock wave, while the tangential component remains unchanged ($u_{t_1} = u_{t_2}$). Therefore, from trigonometry,

$$\tan \epsilon = \frac{u_{n_1}}{u_{t_1}} \tag{7}$$

and

$$\tan(\epsilon - \delta) = \frac{u_{n_2}}{u_{t_2}} \tag{8}$$

or

$$\frac{u_{n_2}}{u_{n_1}} = \frac{\tan(\epsilon - \delta)}{\tan \epsilon} \tag{9}$$

Then, from continuity,

$$\frac{u_{n_2}}{u_{n_1}} = \frac{\rho_1}{\rho_2} \tag{10}$$

or

$$\frac{\rho_1}{\rho_2} = \frac{\tan(\epsilon - \delta)}{\tan \epsilon} \tag{11}$$

With equation (11) substituted in equations (5) and (6), the remaining quantities for a given amount of flow turning, δ, are shock angle, ϵ, and static pressure ratio, p_2/p_1.

The programed iterative process consisted of selecting a trial value of ϵ, calculating the static pressure ratio with both equations (5) and (6), and comparing the two values. A new trial value of ϵ was then selected by linear interpolation and the process was repeated. When the computed difference in the two values of static pressure ratio was within 0.001 percent, the solution was considered satisfactory. Once the pressure ratio and shock angle were found, the Mach number behind the shock, M_2, and the static temperature ratio, T_2/T_1, were determined from the following equations (8).

$$M_2 = \left[\frac{1 + \frac{\gamma - 1}{2} M_1^2 \sin^2\epsilon}{\left[\sin^2(\epsilon - \delta)\right]\left[\gamma M_1^2 \sin^2\epsilon - \frac{\gamma - 1}{2}\right]} \right]^{1/2} \tag{12}$$

$$\frac{T_2}{T_1} = \frac{\left[2\gamma M_1^2 \sin^2\epsilon - (\gamma - 1)\right]\left[(\gamma - 1)M_1^2 \sin^2\epsilon + 2\right]}{(\gamma + 1)^2 M_1^2 \sin^2\epsilon} \tag{13}$$

Swept-Wedge Compression Surface

Referring to figure 6, the geometry of the compression surface is specified by the sweep angle, α, and the ridge angle, β. The compression surface is, therefore, the triangular surface BEO, with $\overline{OE}$ being the horizontal leading edge.

While Mach number is not a vector, it is assumed that the Mach number can be broken into two components. The free-stream Mach number, M_1, is parallel to the x-axis, and the Mach number component normal to the leading edge, M_{N_1}, becomes equal to $M_1 \cos \alpha$.

For the calculations a free-stream Mach number "vector" was assumed to intersect the leading edge at point G such that line $\overline{CG}$ would be perpendicular to the leading edge, $\overline{OE}$. A plane was passed through point G perpendicular to the leading edge containing $\overline{CG}$ and the normal turning angle, δ_N.

The oblique shock wave procedure discussed in the previous section was used to apply δ_N to M_{N_1}, and the flow properties behind the shock wave were calculated. The tangential Mach number, M_{T_2}, was less than M_{T_1} by the square root of the static temperature ratio, $\sqrt{T_2/T_1}$. Also calculated was the normal shock angle, $\measuredangle$ JGC. From the normal and tangential Mach number components behind the shock wave, M_{N_2} and M_{T_2}, the resultant Mach number, M_2, was determined.

Line $\overline{OI}$ represents the resultant Mach number translated over the wedge surface to point O, and the region which must be filled by the plow becomes JIOB. By projecting $\overline{OI}$ down to the xy plane, the amount

of cross-flow, λ, was calculated and the normal shock angle, $\sphericalangle$ JGC, was transferred to the xz plane to produce the ridge shock angle, ω.

The various angles and line segments needed for the solution were determined from trigonometry, utilizing the laws of cosines and sines. This was to keep the solution general and to insure that problems with the leading edge other than horizontal could be solved.

Computed results for a swept wedge.- The computed solution for a swept wedge representing the experimental model ($\alpha = 55^{\circ}$, $\beta = 8^{\circ}$) in a Mach 4.03 flow field is presented in figure 7. These computations are compared to the experimental model in Chapter IV. The solution for an unswept 8° wedge (14) is also given in figure 7 and serves to illustrate that sweeping the leading edge by 55° did not have a great effect on compression (M_2 changed from 3.45 to 3.42). Of greatest significance was the 4.6° of cross-flow and the increase in the shock wave angle from 20.34° to 24.20°.

Parametrics.- Although the geometry of the experimental model was fixed, the appendix presents a study of the parameters which describes a swept wedge. The sweep angle and ridge angle are discussed in regard to their influence on Mach number, static pressure, cross-flow, and shock wave structure. Dihedral, which permits the leading edge to be lifted out of the xy plane, is also introduced. Limitations to the analysis are discussed and, because the amount of sweep is restricted by the analytical computation, the maximum sweep angle is given in the appendix for several swept-wedge configurations.

Center Region Calculation

Figure 8 illustrates how the shock wave structure might appear if the shock waves from each side of the compression surface intersected and remained planar as they extended on to the surface. The numbers in circles indicate the three different flow regions or bays as viewed in the xy plane, while the numbers in squares indicate the three regions as viewed in the yz plane. This nomenclature is given to help identify the three flow regions regardless of whether the flow on the compression surface or the shock wave structure is being considered.

Because each side of the compression surface turned the flow toward the model's plane of symmetry, a complex flow region was expected, beginning at the model's fork. The direction-of-flow arrows show the flow turned back parallel to the plane of symmetry in the center region (region 3), and this is the assumption made to locate the intersection of the shock waves with the compression surface. Therefore, M_2 is subjected to this compression to obtain center region properties and the shock wave angle measured on the compression surface, ϵ_c.

Computed results for the center region.- The cross-flow angle ($\lambda = 4.6^\circ$) is not the exact amount of turning required to bring the flow back parallel to the plane of symmetry because λ is measured in the xy plane. However, the correction to the flow on the compression surface, which is slanting toward the center, is small and has been ignored.

The computed results presented here are compared to the experimental model in Chapter IV. For $M_2 = 3.42$ and $\lambda = 4.6^\circ$, the static

pressure ratio, p_3/p_2, is 1.47 and $\epsilon_c = 15.7^o$. The ratio of pitot pressure in region 3 to static pressure in region 2, P_{p3}/p_2, is 29.2. These conditions can be transferred back to the free stream to become $P_3/p_1 = 3.24$ and $P_{p3}/p_1 = 43.0$.

It is realized that the flow in the center region is more complex than pictured here, but these results should at least serve to approximately describe this region. Two questions arise which are not answered by this analysis of the center region but are discussed in Chapter IV. First, since the two shock waves produced by the leading edges are not strictly of opposite families, would they join in a different manner over the compression surface? And second, what happens to the shock wave after it strikes the compression surface?

CHAPTER IV

RESULTS AND DISCUSSION

The experimental model represents the initial compression surfaces, excluding the vehicle forebody and inlet cowl of a hypersonic inlet. Therefore, the effect of the swept leading edges on static pressure and shock structure are important, as is the requirement of identifying any regions of flow which could contribute to undesirable pressure losses.

Static Pressure Distribution on Compression Surface

The static pressure distribution on the compression surface is presented in figure 9, where L is the length of the model from the fork to the trailing edge and W is the compression surface half-width (see fig. 4). The static pressure profiles in the y-direction are shown in figure 9(a) for three s/L stations. The line indicating where the plow intersects the compression surface is shown to give perspective to the nondimensionalized y/W scale.

Apart from the center region, the pressure is constant across the compression surface and slightly higher than the theoretical calculation discussed in Chapter III. This could be caused by non-uniformities in the test section flow field or the difficulty encountered with accurately measuring low static pressures of 1.0 newton/centimeter. The static pressure taps used to check on symmetry indicated almost no model misalignment and their data are not shown. The most probable reason for the higher static pressure was the fact that the calculated

value had not been corrected for a boundary layer on the compression surface. Such a connection would make the compression surface appear steeper to the approaching flow and result in more compression. For example, the solid line on figure 9(a) represents the calculated static pressure for a wedge ridge angle, β, equal to 9° instead of 8°.

The calculated static pressure for the center region, discussed in Chapter III, was generated with a wedge ridge angle, β, equal to 8° which produces 4.6° of cross-flow. The experimental data show the static pressure rise in the center region influencing a greater part of the compression surface as s/L is increased. This is possibly due to the thickening of the compression surface boundary layer, spreading out the effect of the intersecting shock wave. The location of the center region boundary on the compression surface is discussed in the section entitled "Visual and Flow Analysis." The calculated boundary of the center region on the compression surface tends to underpredict the influence of the center region as s/L is increased. This boundary would be moved outward slightly if a larger β, which generates an increase in cross-flow, were assumed.

Figure 9(b) shows the static pressure distribution on the compression surface both down the model centerline ($y/W = 0$) and $y/W = 0.57$. For the stations of s/L at or ahead of the fork, the static pressure is near the calculated value. The increase in static pressure farther back from the leading edge indicates a small amount of compression has occurred along the surface of the swept wedge.

The dashed lines are the calculated static pressures in region 2 and in the center region, assuming 4.6° of cross-flow.

At the s/L equal to 0.8, the value of p/p_1 has decreased, indicating the possible presence of an expansion region feeding upstream through the subsonic boundary layer from the model's trailing edge.

Shock Wave Structure

Pitot pressure profiles.- Pitot probe surveys are shown in figures 10 and 11 and their results are shown by the contour map of figure 12. The distance from the model fork to the probe tip, s, is measured down the center of the compression surface. The probe was moved vertically, first in the model center plane (fig. 10(a)) and then at stations away from the model center plane until y/s equaled ± 0.191 (fig. 10(f)). Values of $\pm y/s$ are shown to verify shock wave symmetry about the model's plane of symmetry. Surveys for the different probe stations coincided when nondimensionalized with the probe tip distance from the fork, s, indicating the presence of a conical-like flow field in the center region.

Total pressure will decrease behind an oblique shock, but the total pressure loss of the normal shock in front of the probe ahead of the oblique shock is greater than for the combined total pressure loss of the oblique shock and the normal probe shock behind the oblique shock. This characteristic is due to the lower Mach number which exists behind the oblique shock wave. Therefore, the pitot pressure will increase when the probe moves behind an oblique shock wave. The

parameter P_p/p_1 is the local pitot pressure divided by the free-stream static pressure.

Pitot pressure is presented instead of total pressure because of the non-uniform flow field found in the center region. Small changes in static pressure have a great influence on total pressure calculations, and no static pressure data were taken above the compression surface. Therefore, instead of adjusting the pitot pressure by a calculated static pressure, the experimental pitot pressure data is presented and compared to the pitot pressure obtained from the theoretical calculations.

The value of P_p/p_1 equal to 21.4 corresponds to a free-stream Mach number of 4.03. The calculated value of P_p/p_1 in region 2 is 34.2, but region 2 was not seen by the pitot probe until y/s was greater than ± 0.068 (see figs. 10(c) - 10(f)). The average Mach number in region 2 was found from the average experimental values of P_{p_2} and p_2 to be 3.30, which is 4 percent less than the calculated value. This increased compression was consistent with the boundary-layer growth on the compression surface.

In the center region, or region 3, the experimental P_p/p_1 was approximately equal to the calculated value of 40.3, but the non-uniformity of the flow field is evident from the varying pitot pressure. Normally there was a decrease in pitot pressure as the pitot probe moved closer to the model in the center region when y/s was equal to or greater than ± 0.068. One exception was in the survey closest to the model's fork ($s = 4.45$ centimeters) for $y/s = +0.137$ (see fig. 10(e)).

Three yaw surveys of the pitot probe presented in figure 11 were made above the intersection of the shock waves from the leading edge. The value of $P_p/p_1 = 21.4$ near $y/s = 0$ is for the free stream and $P_p/p_1 = 34.2$ is for region 2 where the pitot probe moved behind the leading-edge shock waves. There was no appreciable drop in pressure as $\pm y/s$ increased in either region 1 or region 2, indicating no noticeable error from probe misalignment due to increased yaw.

Lateral pitot surveys with approximately the same value of z/s coincided even though the value of s changed. This would be expected if the shocks from the leading edges were planar. An average calculated curve is shown for z/s between 0.398 and 0.405, as the difference is small. There is a greater distance between the leading-edge shock waves for $z/s = 0.462$, but all three yaw surveys indicate the leading-edge shock waves are closer together at their respective stations than the calculated results predict.

The small symbols with dots in figure 12 locate the shock waves as determined from the vertical pitot probe surveys seen in figure 10. Vertical instead of lateral surveys were used as the probe was more perpendicular to the shock waves and could more easily distinguish the different regions.

While figures 10 and 11 show the experimental pitot pressure for the three regions to be near the calculated value, figure 12 indicates why the locations of the regions were not correctly predicted. First, the leading-edge shock waves were located above the calculated position for $\beta = 8^\circ$. The shock structure for $\beta = 9^\circ$, which provided a boundary

layer displacement thickness correction, was nearer the experimental results. Second, the shock waves from the leading edge did not intersect along a line in the xz plane but instead were joined by a shock wave perpendicular to the xz plane.

The joined shock wave made the shock structure appear much like that of the corner-flow problem. In fact, pitot pressure contours in the entire center region were similar to that of the corner-flow problem discussed experimentally in reference 15 and analytically in reference 16. For the experimental model, the corner angle would be highly obtuse (157°) and the leading edges swept forward from the corner (fork).

The angle the joined shock wave made with the free-stream flow was found to be 26.6° measured in the xz plane, which is the angle of a two-dimensional shock wave contributing 14.7° of turning to a Mach 4.03 flow. This flow turning yields P_{p_3}/p_1 equal to 43.1 and is approximately the computed value for the center region. Therefore, by reversing the process, it would have been possible to approximately locate the joined shock wave with the calculated pitot pressure in the center region. This does neglect the boundary-layer considerations previously discussed.

Visual and Flow Analysis.- The photograph in figure 13 was taken immediately after the oil-streak test was made. Initial movements, about one-third the length of most streaks, would have occurred before the test section obtained supersonic flow and should be ignored. Outside the center region, the streaks show the flow parallel to the lines of intersection between the compression surface and the plows. The leading edges of the plows were designed to follow the shock waves

produced by the compression surface and, as expected, there was no evidence of any shock wave on the plows. This indicates the waves fell very near the plow leading edges as designed or somewhere above the model.

The edge of the center region is visible in the oil-streak photograph and indicates the flow had been turned back parallel to the model's plane of symmetry. In fact, it appears that the flow was turned more than just parallel and produced a spreading effect. This is believed to be caused by the oil following the direction of the subsonic sublayer of the boundary layer instead of the inviscid flow field. This boundary layer would have the tendency to flow away from the high-pressure center region.

From the oil-streak data, the boundaries of the center region on each side of the compression surface were found to form angles of between 15° and 17° with the model plane at symmetry. These positions are represented by the diamonds in figure 12 and compare to the calculated value of ϵ_c equal to 15.7°.

Beyond the maximum yaw position of the pitot probes ($y/s = \pm 0.091$), the shock wave structure is shown in figure 12 to be extrapolated to the compression surface at the points determined from the oil-streak data. The shock waves were assumed to be perpendicular to the surface as there was no evidence from the static pressure, pitot pressure, or oil-streak data that the shock wave reflected from the surface back toward region 3. This was consistent with reference 17 which deals with a limiting case for corner flow. If the shock wave reflected into

region 2, it would violate the restriction that disturbances in supersonic flows cannot lie ahead of the Mach angle.

Because the calculated boundary of the center region was represented by a planar shock wave extending from the shock wave intersection point to the compression surface, it greatly underpredicted the area of influence of the center region. The compression surface boundary to the area of influence of the center region felt by static pressure is marked by the square symbol in figure 12. This point was determined from an interpolation of the three axial stations of figure 9(a), and fell outside both the calculated boundary and the boundary indicated by the oil-streak data.

Figure 14(a) is a no-flow schlieren photograph and is presented to help identify the distinguishing features found in figure 14(b) where $M_1 = 4.03$. The region along the top of the photograph is the test section boundary layer which has grown considerably over the distance from the nozzle throat. The one oblique shock wave is from the leading edge of the flat plate which spans the test section. Substantiating the plow design is the fact that there are no other visible shock waves which could have originated within the model.

All the data verified the conical-like flow field within the center region, as it was possible to obtain a correlation by using the nondimensionalized distance from the fork, s. However, the lines of intersection of the two plows with the compression surface approach the plane of symmetry as s is increased. Therefore, in keeping with the scale of the model, figure 12 was constructed for s equal to 1/2 L.

At this station, the experimental center region represents 4 percent of the model frontal area and is a region of highly disturbed flow which could prove undesirable if not unacceptable in the throat of a hypersonic inlet.

CHAPTER V

CONCLUDING REMARKS

The flow field of a swept-wedge model, representing the initial compression surface of a hypersonic inlet, was investigated and compared with theory. The leading edges of the two wedges of the experimental model were swept back toward each other, which turned the flow toward the model's plane of symmetry. A uniform flow field was found except in the model's center region.

In the center region there existed a flow and shock wave structure similar to the corner-flow problem with the corner angle equal to 157°. The shock waves generated by the leading edges were joined together by a shock wave perpendicular to the model's plane of symmetry. The shock waves were then bent around the center region to become perpendicular to the compression surface. The center region represented approximately 4 percent of the model's frontal area when measured at a station half way down the center of the compression surface from the leading edge. This region of conical-like three-dimensional flow would be a large percentage of the flow in the throat of a hypersonic inlet and should be a design consideration.

By breaking the free-stream flow into velocity components normal and tangential to the leading edges, a two-dimensional analysis was used to determine shock wave structure and flow properties. The analysis was improved when plows were used on the experimental model to fill the region left by the cross-flow generated by the swept

compression surfaces. By turning the cross-flow parallel to the model's plane of symmetry, the location of the shock wave intersections on the compression surfaces was determined. However, this assumption underpredicted the size of the center region as it does not consider the forming of a third wave between the leading-edge shock waves. Also, there was no provision for the three-dimensional flow which existed in the center region.

The calculated and experimental values of pitot pressure and shock wave structure outside the center region were in good agreement. There was some underprediction of the static pressure and the angle the leading-edge shock wave made with the compression surface. This was attributed to compression from boundary-layer growth on the model's surface. The experimental value of Mach number behind the leading-edge shock waves was approximately 4 percent less than the calculated value of 3.42.

REFERENCES

1. Eggers, A. J., Jr.; Petersen, R. H.; and Cohen, N. B.: Hypersonic Aircraft Technology and Applications. Astronautics and Aeronautics, vol. 8, no. 6, June 1970, pp. 30-41.

2. Anon.: Statement of Work, Hypersonic Ramjet Experiment Project for Phase I. Langley Research Center, L-4947, Hampton, Va., 1965.

3. Henry, J. R.; and McLellan, C. H.: The Airbreathing Launch Vehicle for Earth Orbit Shuttle - New Technology and Development Approach. AIAA Advanced Space Transportation Meeting, Cocoa Beach, Florida, Feb. 4-6, 1970.

4. Faro, Ione D. V.: Supersonic Inlets. North Atlantic Treaty Organization Advisory Group for Aerospace Research and Development, AGARDograph 102, May 1965.

5. Dunsworth, L. C.; and Woodgrift, R. E.: An Inlet for the Dual Mode Scramjet. AIAA Third Propulsion Joint Specialist Conference, Washington, D.C., July 17-21, 1967.

6. Anon.: Investigation of the Low Speed Fixed Geometry Supersonic Combustion Ramjet. General Applied Science Laboratories, Inc., AFAPL-TR-66-139, March 1967.

7. Torrence, M. G.: Concentration Measurements of an Injected Gas in a Supersonic Stream. NASA TN D-3860, Washington, D.C., April 1967.

8. Ames Research Staff: Equations, Tables, and Charts for Compressible Flow. NACA Report 1135, Washington, D.C., 1953.

9. Liepmann, H. W.; and Roshko, A.: Elements of Gasdynamics. John Wiley and Sons, Chapter 6, 1957.

10. Hilliard, E. E.: Supersonic Wind Tunnel Tests of Several Pitot-Static Probes. Arnold Engineering Development Center, Arnold Air Force Station, Tenn., 1965.

11. Mascitti, V. R.: A Closed-Form Solution to Oblique Shock-Wave Properties. J. Aircraft, vol. 6, no. 1, Jan.-Feb. 1969, p. 66.

12. Schapiro, A. H.: The Dynamics and Thermodynamics of Compressible Fluid Flow. Vol. I, Ronald Press Co., Chapter 16, 1953.

13. Moeckel, W. E.: Oblique-Shock Relations at Hypersonic Speeds for Air in Chemical Equilibrium. NACA TN 3895, Washington, D.C., Jan. 1957.

14. Dennard, J. S.; and Spencer, P. B.: Ideal-Gas Tables for Oblique-Shock Flow Parameters in Air at Mach Numbers From 1.05 to 12.0. NASA TN D-2221, Washington, D.C., March 1964.

15. Charwat, A. F.; and Redekopp, L. G.: Supersonic Interference Flow Along the Corner of Intersecting Wedges. AIAA Journal, vol. 5, no. 3, March 1967, pp. 480-488.

16. Rubin, S. G.; and Grossman, B.: Viscous Flow Along a Corner, Part II - Numerical Solution of Corner Layer Equations. Polytechnic Institute of Brooklyn, Dept. of Aerospace Engineering and Applied Mechanics, PIBAL Report No. 69-33, Aug. 1969.

17. Korkegi, R. H.: Limit Case for Supersonic Inviscid Flow in the Corner of Intersecting Wedges. AIAA Journal, vol. 7, no. 3, March 1969, pp. 569-570.

18. Roffe, G.: Techniques for the Analysis of Three-Dimensional Effects in Supersonic Inlets. General Applied Science Laboratories, Inc., GASL-TR-616, 1966.

19. Trimpi, R. L.; and Jones, R. A.: A Method of Solution With Tabulated Results for the Attached Oblique Shock-Wave System for Surfaces at Various Angles of Attack, Sweep, and Dihedral in an Equilibrium Real Gas Including the Atmosphere. NASA TR-63, Washington, D.C., 1960.

20. Ferri, A.: Elements of Aerodynamics of Supersonic Flows. The Macmillan Company, New York, Chapter 3, 1949.

APPENDIX

PARAMETRIC STUDY OF SWEPT WEDGES

Although the experimental model was restricted to one sweep angle and one ridge angle, the theoretical analysis was used to make a parametric study on swept wedges. This study also found some restrictions which must be imposed on the analysis which utilized two-dimensional techniques.

Figure 15(a) shows a wedge of the same class as the experimental model with the leading edge lying in the xy plane. The wedge has been made into a compression ramp on each side of the xz plane in figure 15(b). A plow has been added to fill the void left by the flow turned away from the xz plane. Figure 16 is another swept wedge, characterized by the compression surface having its dihedral line, and hence the compression surface, perpendicular to the xz plane. Therefore, the leading edge is lifted out of the xy plane. Carrying this process another step, the configuration of figure 17 can be developed. This configuration, known as the caret wing, was developed from tracing streamlines in a two-dimensional flow field. No plow is required because the flow is not turned away from the xz plane, and the amount of flow turning is equivalent to the wedge ridge angle.

Reference 18 uses an analysis similar to the one presented here for the horizontal leading-edge wedge, but no parametric results are given. Reference 19 includes real gas effects for different values of γ but presents a coordinate system making it difficult to refer

the downstream flow direction back to the free stream. In addition, the results are presented in terms of the dihedral angle, which changes with sweep angle for the horizontal leading-edge compression surface.

Dihedral parameter.- In this analysis a dihedral parameter, ψ, was used to represent the wedge dihedral instead of the dihedral angle, ϕ. The dihedral parameter is identified in figure 18 to be $\overline{DE}/\overline{AD}$ and is compared to the dihedral angle in figure 19. Control of ψ was easier since the value is zero for the horizontal leading-edge compression surface. Also, regardless of the sweep angle or the ridge angle, the horizontal compression-surface configuration ($\phi = 0.0$) always has a ψ value of 1.0. Both parameters will change for any other leading-edge position including the streamline-traced surface. While the dihedral angle can be either positive or negative as shown in the sketch of figure 19, the value of ψ can vary from zero for the horizontal leading edge to $\tan \epsilon/\tan \delta$ for the streamline-traced configuration. When the leading edge does not lie in the xy plane, line segment $\overline{JC}$ (seen in figs. 6 and 18) does not coincide with $\overline{BC}$, and the normal turning angle becomes $\sphericalangle HGC$ with the plane JGC still required to be perpendicular to the leading edge at point G.

Normal turning angle and Mach number.- For the shock wave to be planar and attached to the leading edge, the Mach number component normal to the leading edge must negotiate the normal turning angle, δ_N. Therefore, δ_N, which is a function of wedge geometry but not Mach number, has been plotted against sweep angle and dihedral for various ridge angles in figure 20. As expected, the angle becomes quite large

at high sweep angles and increased values of ridge angle. However, δ_N is not a strong function of dihedral regardless of the ridge angle except for very large sweep angles. In this and subsequent figures, the circular symbol represents the experimental model. As can be seen, a 2° change in ridge angle of the experimental model has a greater influence on the normal turning angle than a 5° change in sweep angle, while the dihedral has almost no influence. The value of ψ which produces a maximum value for δ_N is 0.5. For large values of sweep angle, the value of δ_N is large but falls off rapidly as the value of ψ for the streamline-traced configuration is approached. The small crosses indicate the streamline-traced configuration for $M_1 = 4.0$.

Figure 21 presents the normal Mach number component as a function of sweep angle and dihedral. The normal Mach number is independent of the ridge angle for the horizontal leading edge but is a function of the sweep angle and the free-stream Mach number. The value of M_{N_1} is equal to unity when the sweep angle is equal to the Mach angle $\left(\sin^{-1}\frac{1}{M_1}\right)$. For Mach 4, with 50°, 55°, and 60° sweep angles, figure 21(b) illustrates that M_{N_1} is insensitive to dihedral and ridge angle.

Maximum sweep angle.- Both an increasing δ_N and a decreasing M_{N_1} contribute to a shock which is detached from the leading edge. Increasing sweep angle drives both parameters toward a detached situation, which two-dimensional techniques can no longer solve because of the three-dimensional flow between the wedge and the bent shock wave.

The maximum shock wave angle, ϵ_{max}, which the flow can produce at any Mach number can be determined from the following equation (20):

$$\sin^2\epsilon_{max} = \frac{1}{\gamma M_1^2}\left[\frac{\gamma + 1}{4} M_1^2 - 1 + \sqrt{(\gamma + 1)\left(1 + \frac{\gamma - 1}{2} M_1^2 + \frac{\gamma + 1}{16} M_1^4\right)}\right]$$

This equation was incorporated in the swept-wedge computer program, and an iterative process was used to determine the maximum sweep angle for a given ridge angle and Mach number resulting in figure 22(a).

The curve with zero ridge angle is a limiting condition for a wedge with zero thickness. Because the normal Mach number component does not change when crossing the leading edge of a zero thickness wedge, the limit occurs when M_{N_1} is equal to unity. The maximum sweep angle would then be equal to the complement of the free-stream Mach angle. The maximum sweep angle increases rapidly with Mach number initially but quickly levels off as the flow becomes hypersonic. For M_1 equal to infinity, the maximum turning a perfect gas can negotiate is 45.6° (8) resulting in a maximum sweep angle of 83° for a ridge angle of 8°. Figure 22(b) illustrates the variation in maximum sweep angle with increasing dihedral.

Theoretically, the sweep angle should extend 90° for the streamline-traced wedge. However, above α_{max} equal to approximately 80°, the value of M_2 generated by the computer program begins to drift away from the correct value. This region of uncertainty is shown by the dashed lines in figure 22(b). There is no explanation for the crossing of the β lines at Ψ equal to 2.0.

Downstream shock wave properties.- The remaining figures in the parametric study (figs. 23 - 26) concern themselves with flow properties behind the shock wave produced by the swept leading edge. The properties have been nondimensionalized by the properties of a two-dimensional wedge to demonstrate the effects of the swept wedge above that of a wedge with zero sweep angle. Two-dimensional wedge properties can be found in reference 14.

Figure 23 indicates the swept-wedge effect on the downstream Mach number. Because of the expanded ordinate, the change in $M_2/M_{2,\alpha=0}$ appears large with change in sweep angle. Actually, changing the ridge angle would have a much greater effect on M_2 than sweep angle. This fact is not apparent on figure 23(a) because $M_2/M_{2,\alpha=0}$ is different for each ridge angle. As sweep angle is increased, the amount of compression increases, resulting in a decrease in M_2 for the horizontal leading-edge wedge at $M_1 = 4.0$. This is not always true, however, because at 55° sweep and 8° ridge angle, M_2 becomes greater than the zero sweep value for Mach numbers greater than 6 (see fig. 23(b)). When the dihedral is varied, the greatest amount of compression occurs for the horizontal compression-surface wedge where the flow is turned by the full amount of the ridge angle plus the cross-flow angle. The amount of compression for the streamline-traced wedge becomes the same as for the zero sweep horizontal leading-edge configuration, where the amount of flow turning is equal to the ridge angle.

Figure 24 is presented because of the importance of being able to locate the shock wave. The angle the shock wave makes with the xy plane

measured in the xz plane is ω. This angle along with the leading edge determines the location of the attached shock wave. While ω climbs radically with increasing sweep angle (see fig. 24(a)), the same geometry produces less of an effect at high Mach numbers, as shown in figure 24(b). The shock wave angle decreases to the two-dimensional value for the streamline-traced wedge (see fig. 24(c)).

The cross-flow angle (λ in fig. 18) is dependent upon sweep angle, ridge angle, dihedral, and Mach number. The amount of cross-flow is a strong function of the nearness to the maximum sweep angle where the cross-flow becomes large. Therefore, higher sweep and lower Mach numbers increase cross-flow (see figs. 25(a) and 25(b)). Increasing the dihedral will reduce the cross-flow angle (see fig. 25(c)) and the streamline-traced surface produces no cross-flow. This property served as a check on the analytical solution because the computer solution followed the same procedure for all cases.

The static pressure rise across the shock wave illustrated in figure 26 indicates the amount of compression obtained by utilizing swept wedges. This figure, along with the result of figure 23, can be used to illustrate that any increased compression, brought about by the swept wedge, accompanies a corresponding decrease in Mach number. This results in a decrease in total pressure recovery. Therefore, no measurable compression benefits are obtained through the use of a swept compression surface with regard to total pressure recovery. Hence, it must be concluded that the greatest benefits of swept-wedge compression surfaces would come from inlet structural and self-starting considerations and not from benefits in increased total pressure recovery.

The vita has been removed from the scanned document

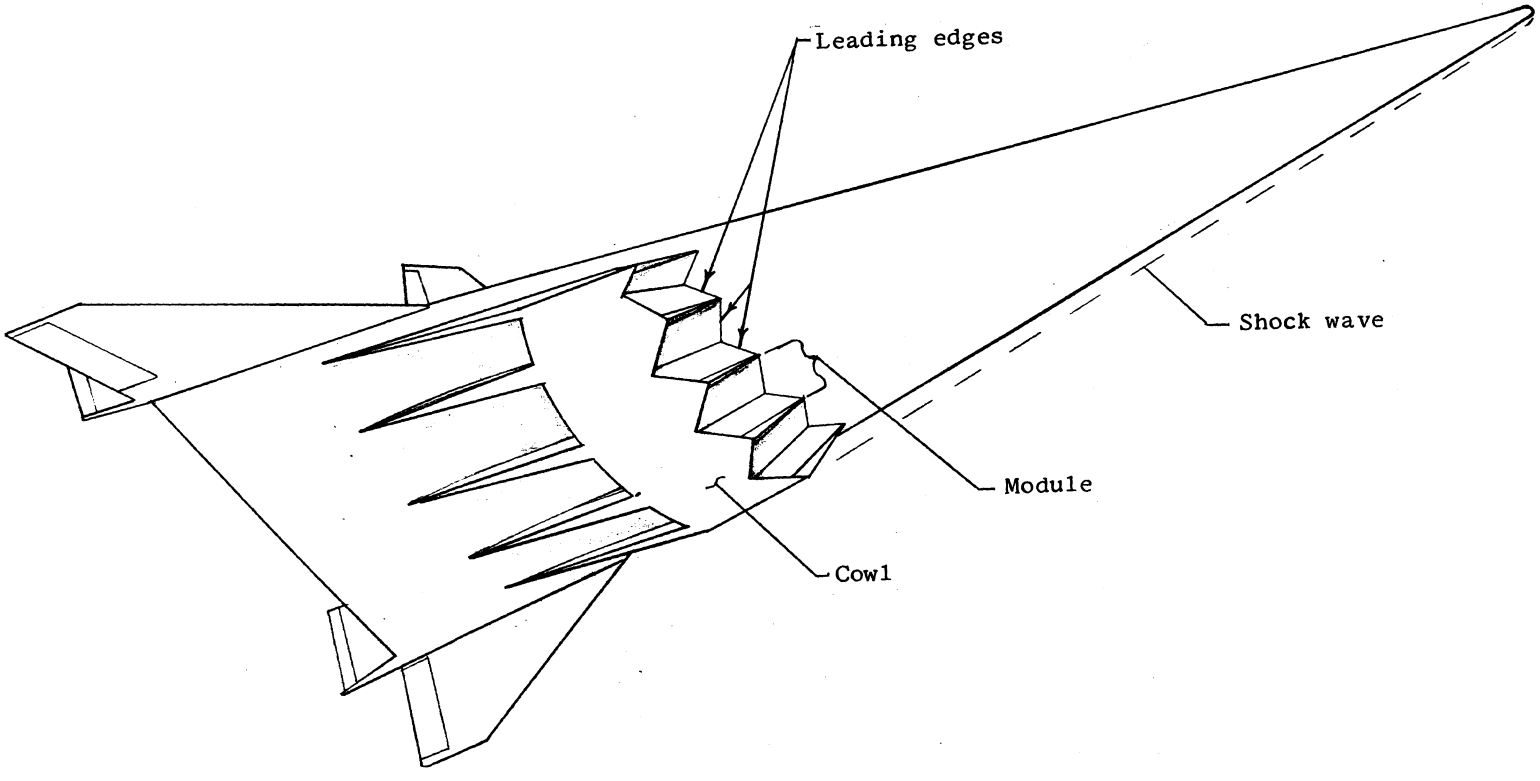

Figure 1.- Hypersonic vehicle.

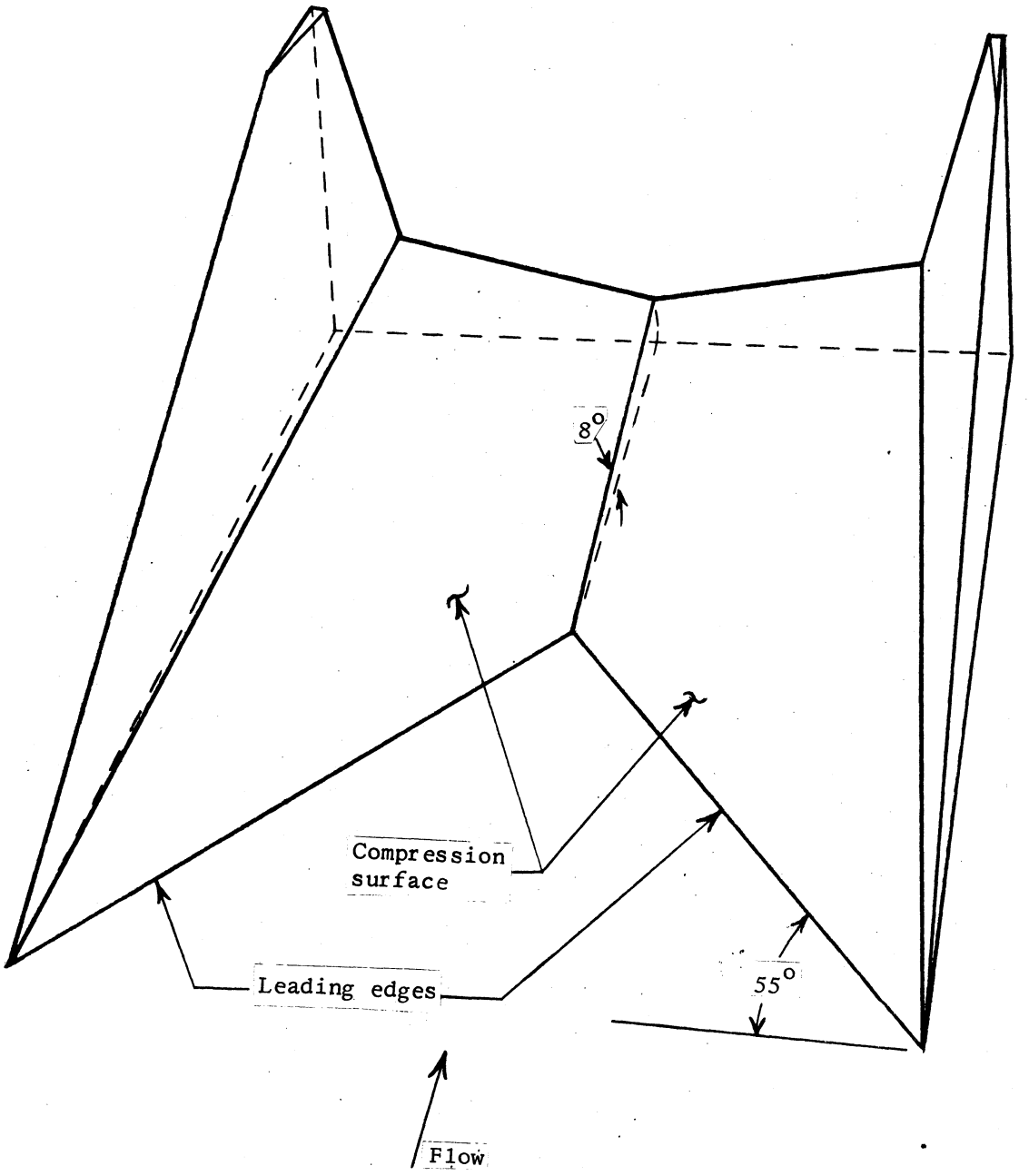

Figure 2.- Swept wedge model.

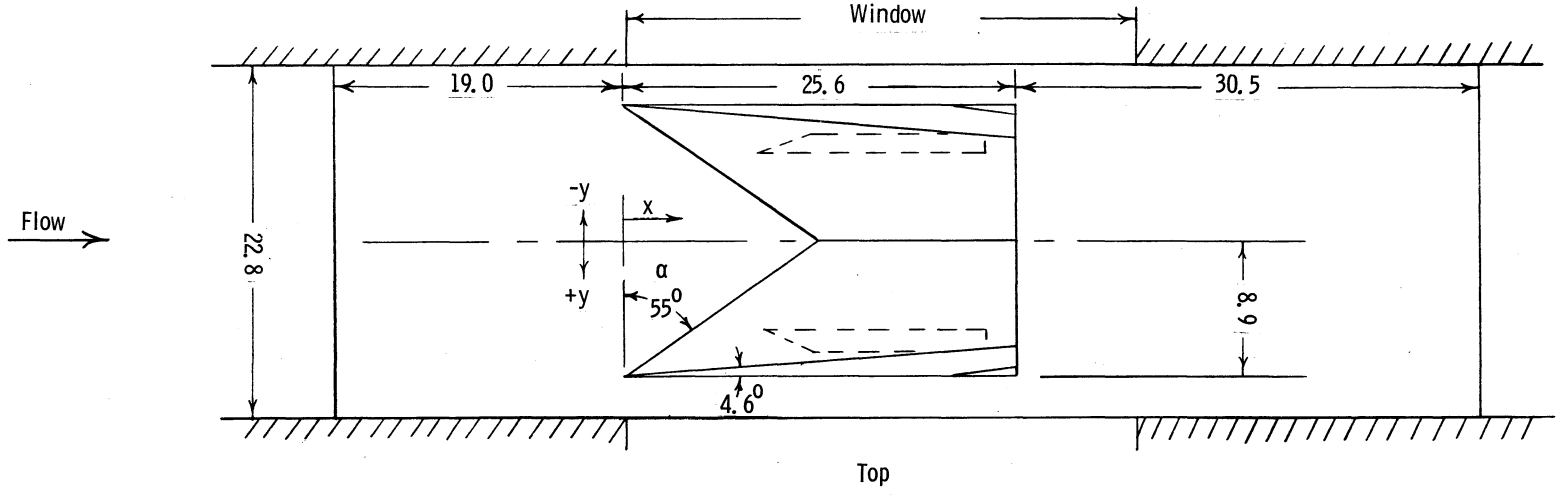

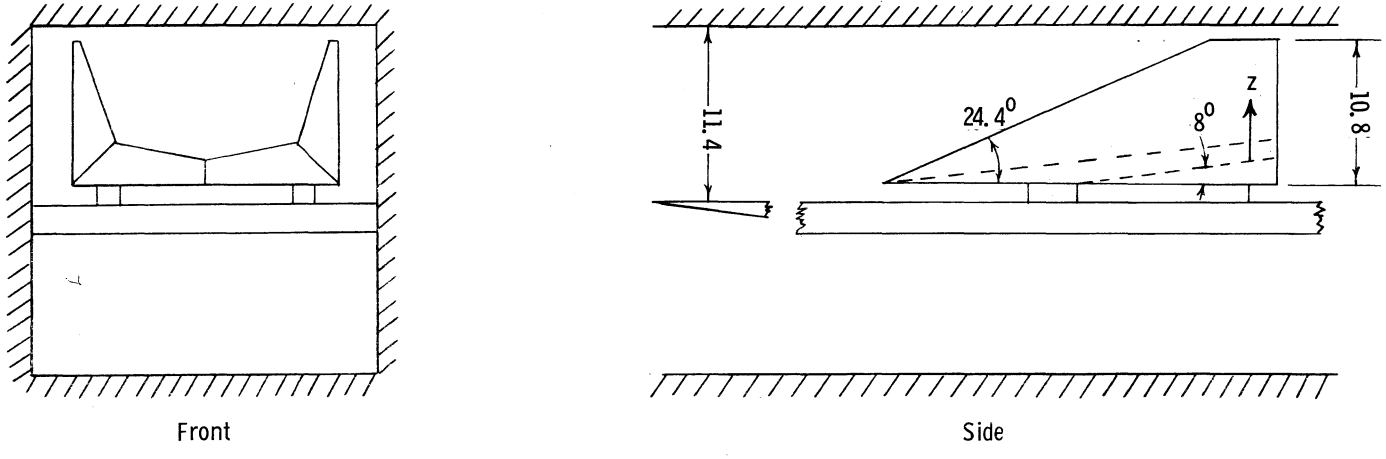

Figure 3.- Sketch of model in Mach 4 channel.

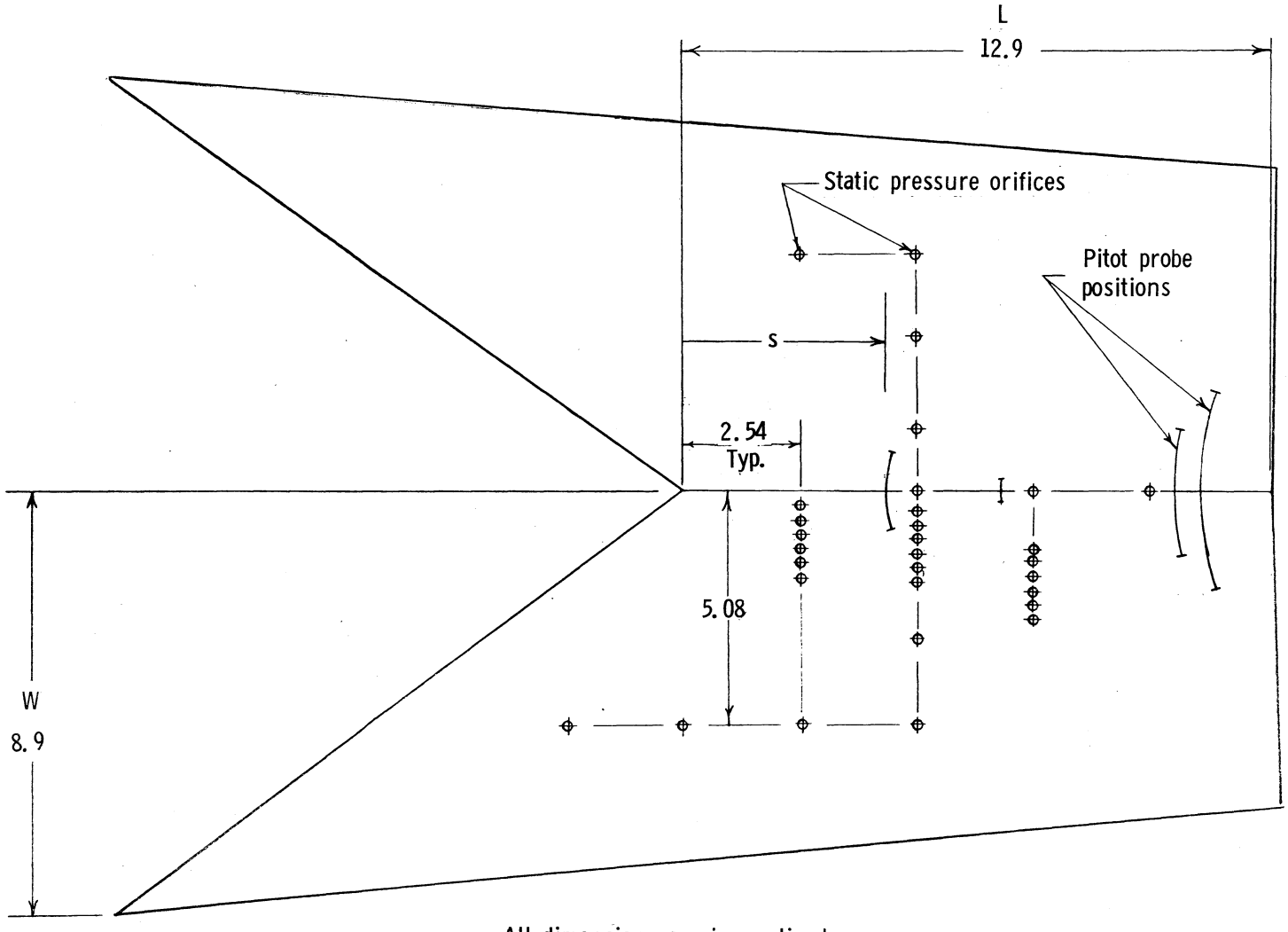

Figure 4.- Model compression surface.

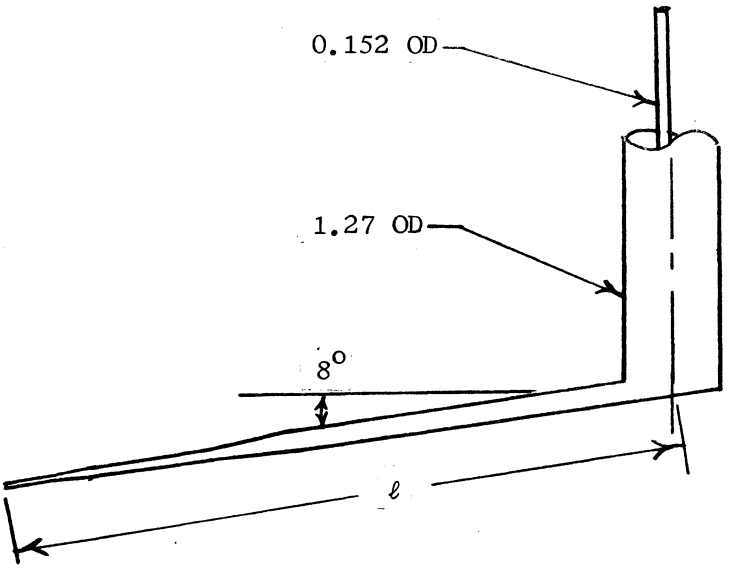

All dimensions are in centimeters

	s	ℓ	Tip
1	4.45	2.54	0.102 OD
2	11.32	7.04	0.102 OD
3	10.77	7.60	0.051 OD
4	7.01	11.36	0.013 0.102

Figure 5.- Pitot probes.

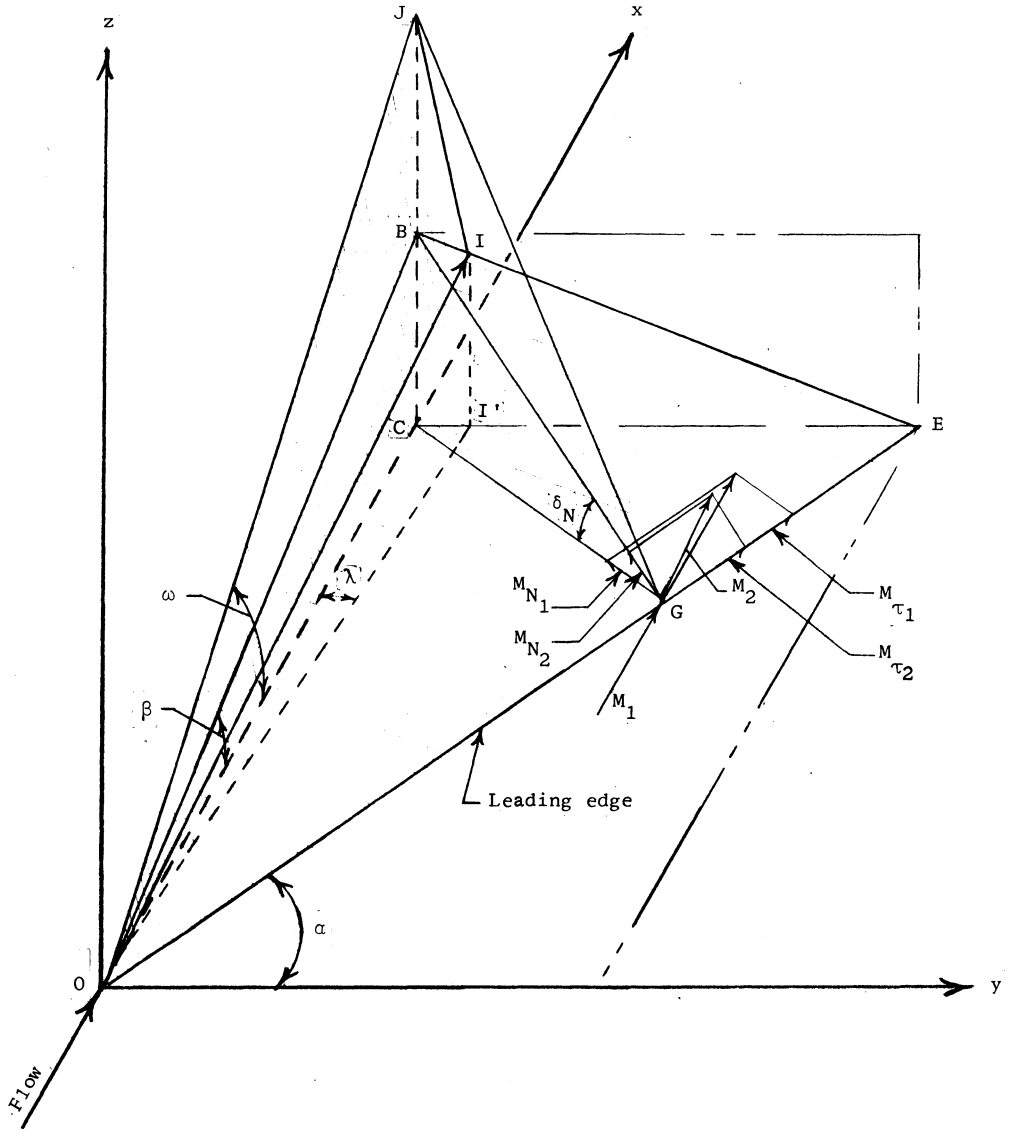

Figure 6.- Mathematical model.

	Experimental model $\alpha = 55^{o}$; $\beta = 8^{o}$ (Theoretical values)	2-dimensional wedge $\alpha = 0^{o}$; $\beta = 8^{o}$
Normal turning angle, δ_N, deg.	13.77	8.00
Normal Mach no. component, M_N	2.31	4.03
Downstream Mach number, M_2	3.42	3.45
Static pressure rise, p_2/p_1	2.20	2.13
Crossflow angle, λ, deg.	4.57	0
Shock wave angle, ω, deg.	24.20	20.34
P_{p_2}/p_1	34.20	33.65

Figure 7.- Calculated properties for two compression surfaces, $M_1 = 4.03$.

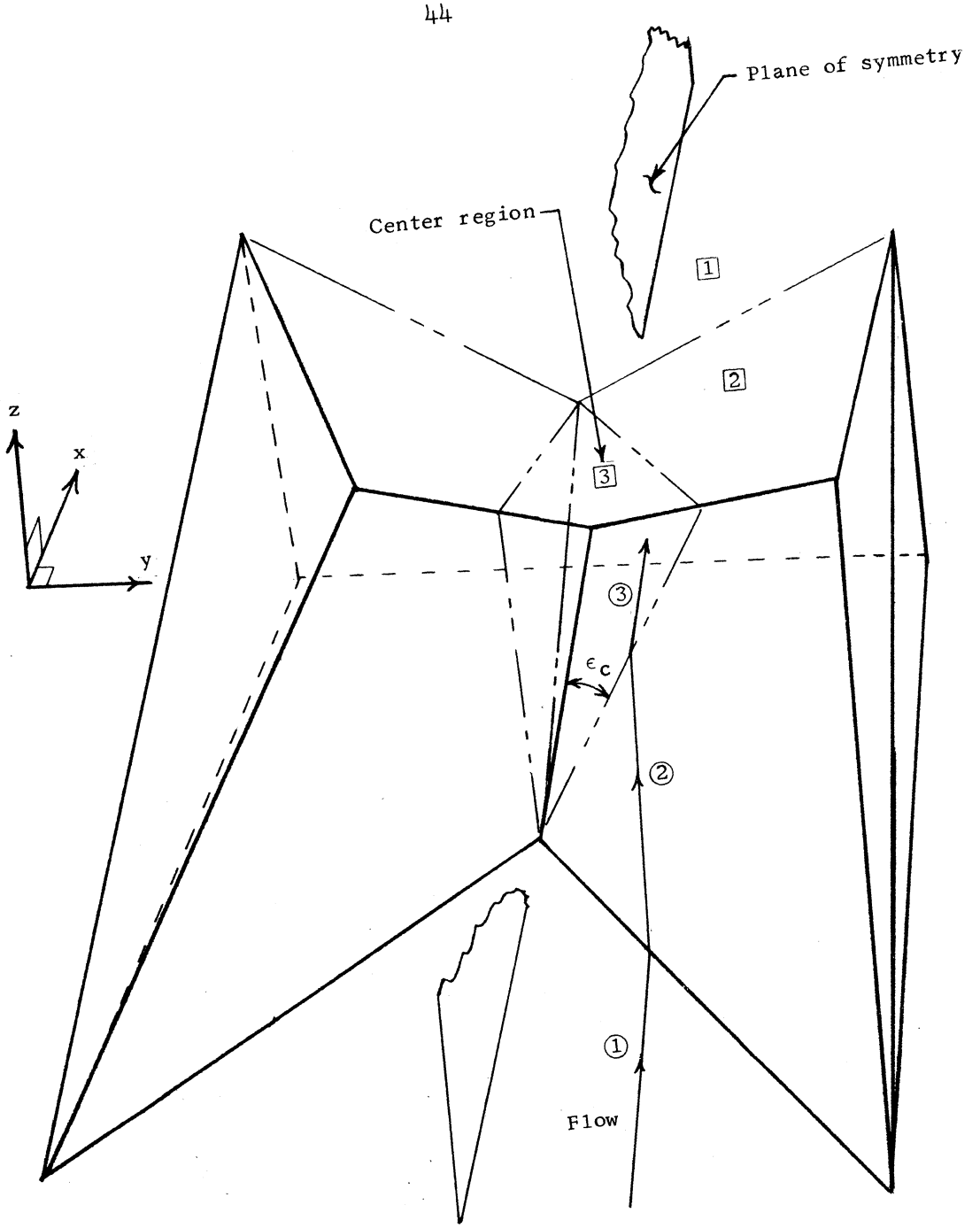

Figure 8.- Shock wave structure.

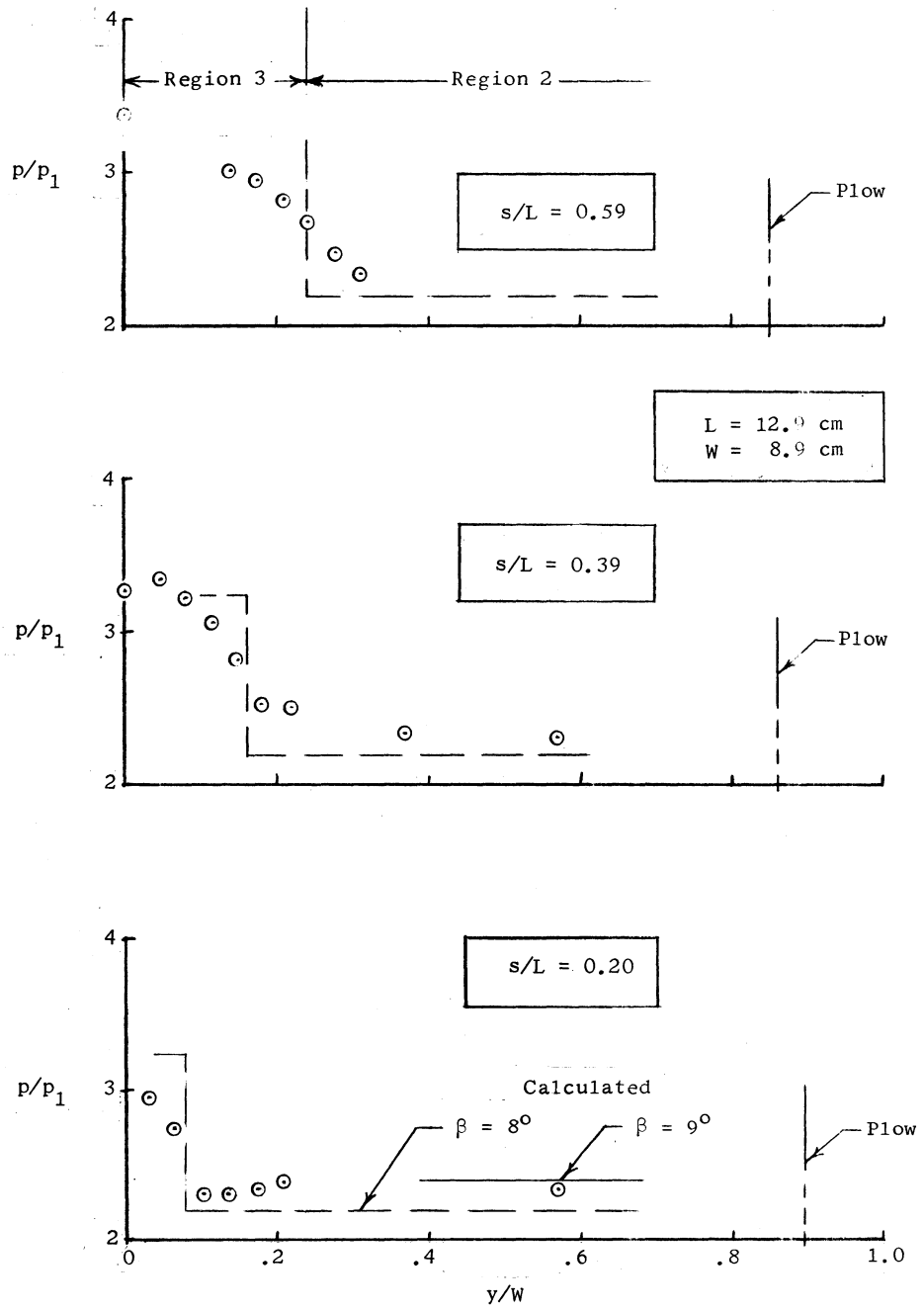

(a) y direction.

Figure 9.- Static pressure distribution on compression surface.

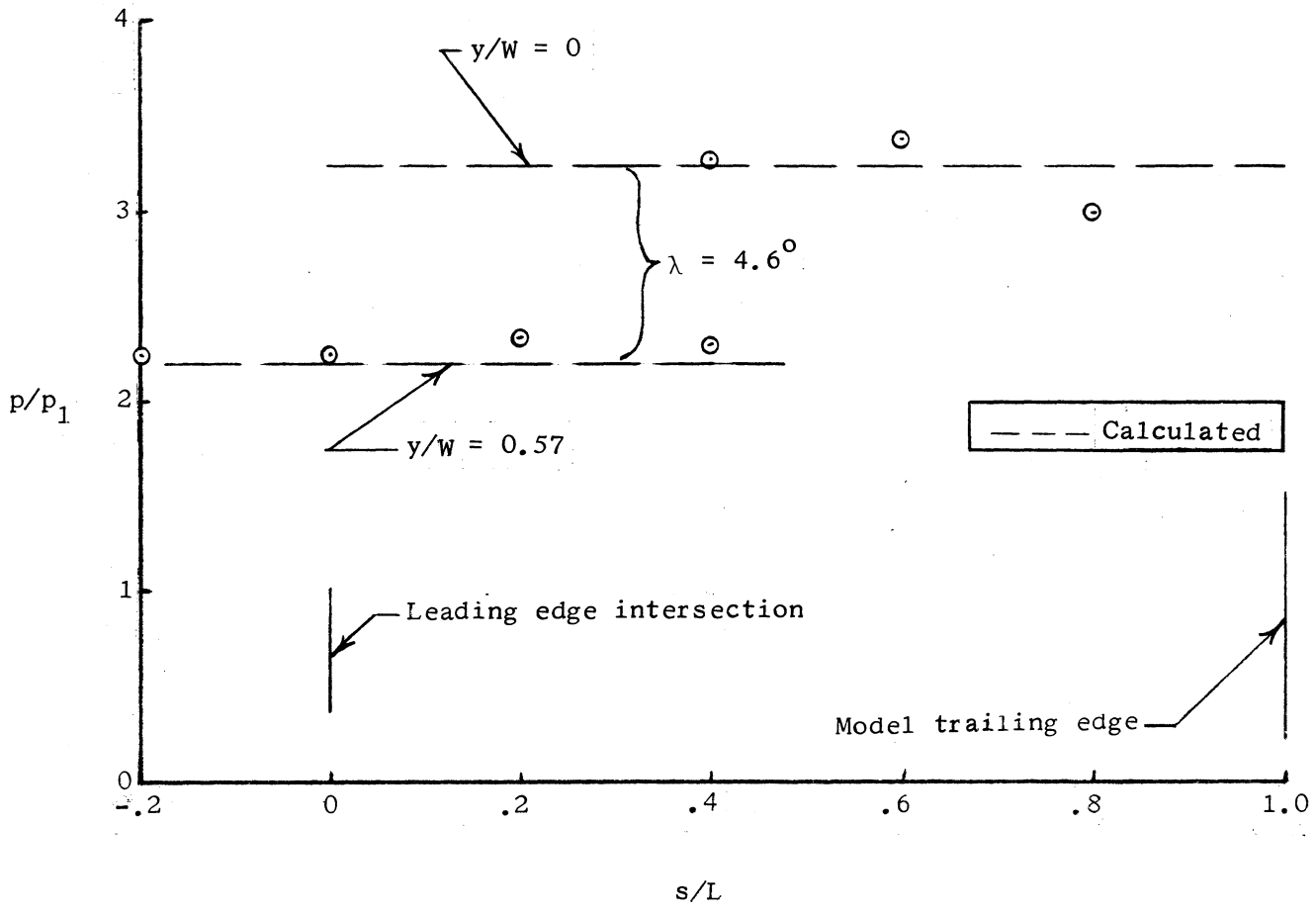

(b) x direction.

Figure 9.- Concluded.

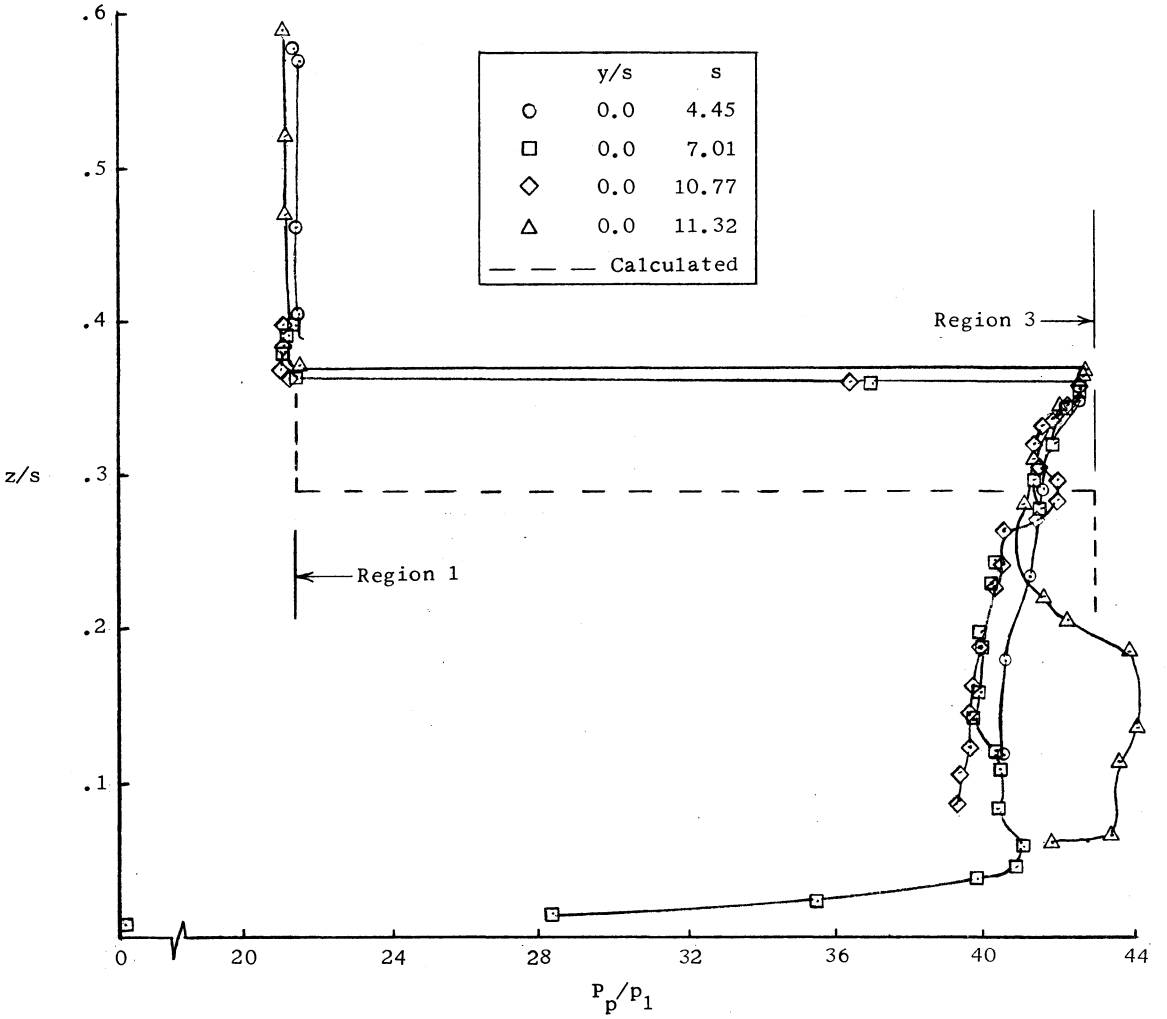

(a) y/s = 0.0.

Figure 10.- Vertical pitot probe surveys.

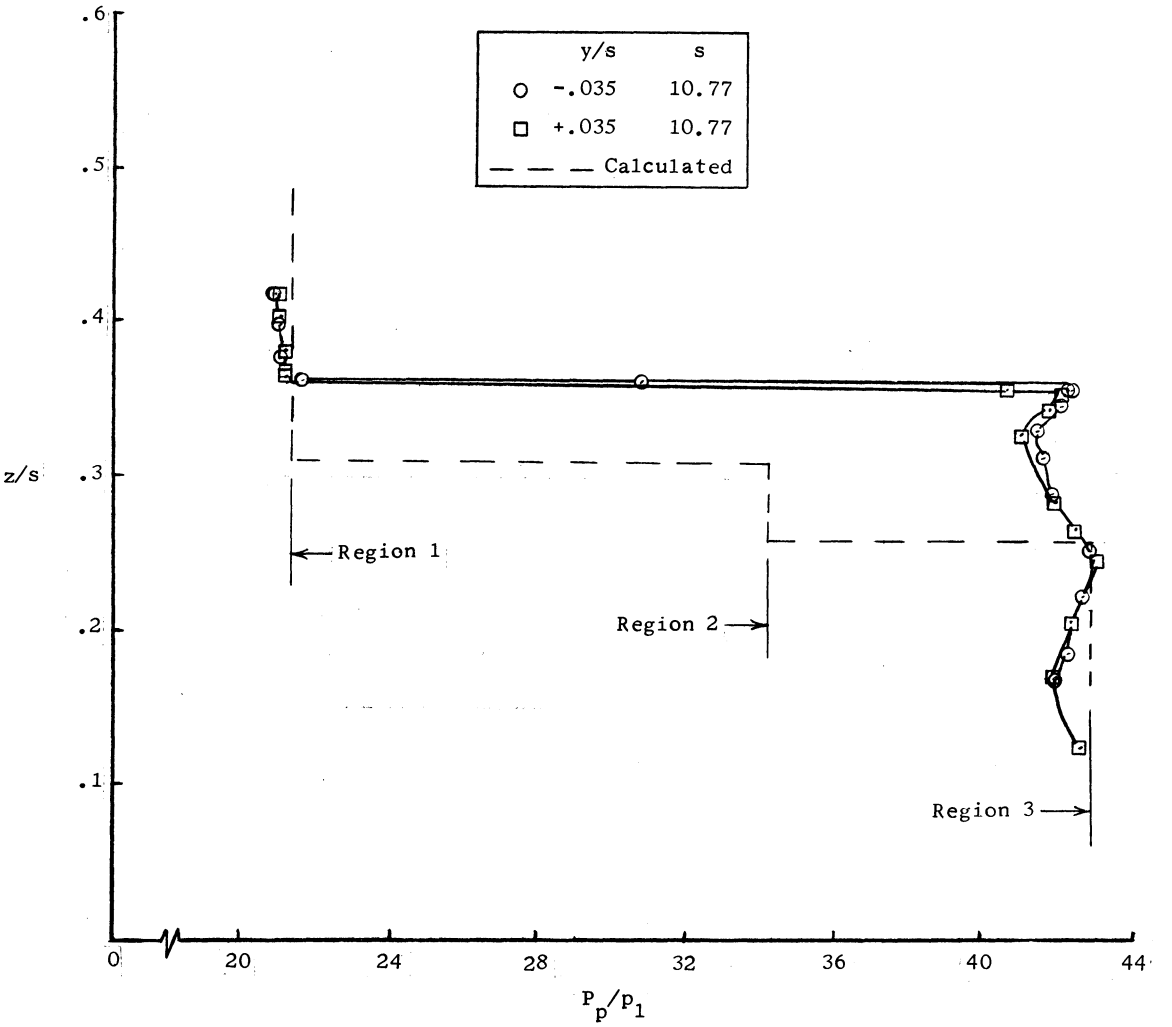

(b) $y/s = \pm 0.035$.

Figure 10.- Continued.

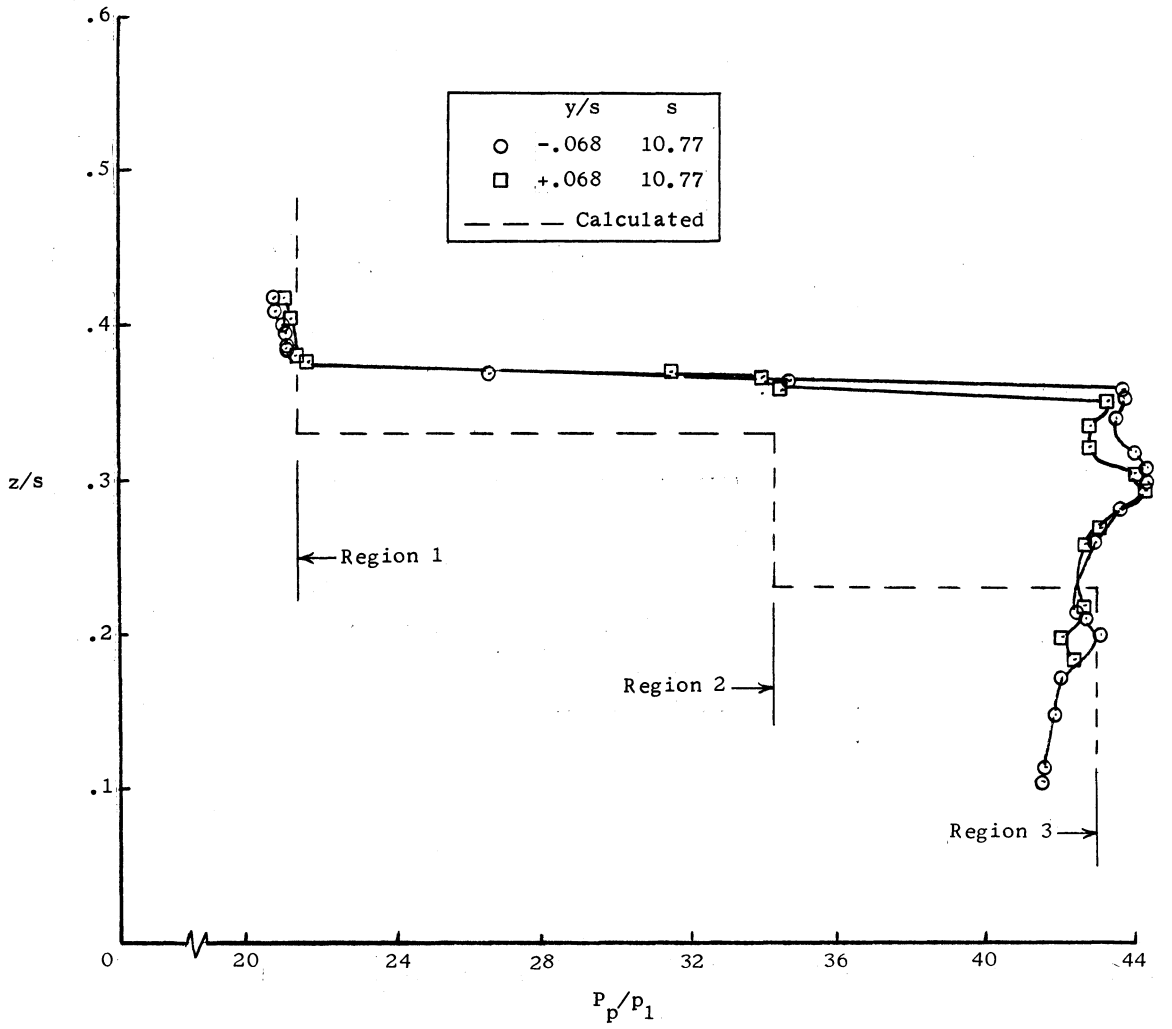

(c) $y/s = \pm 0.068$.

Figure 10.- Continued.

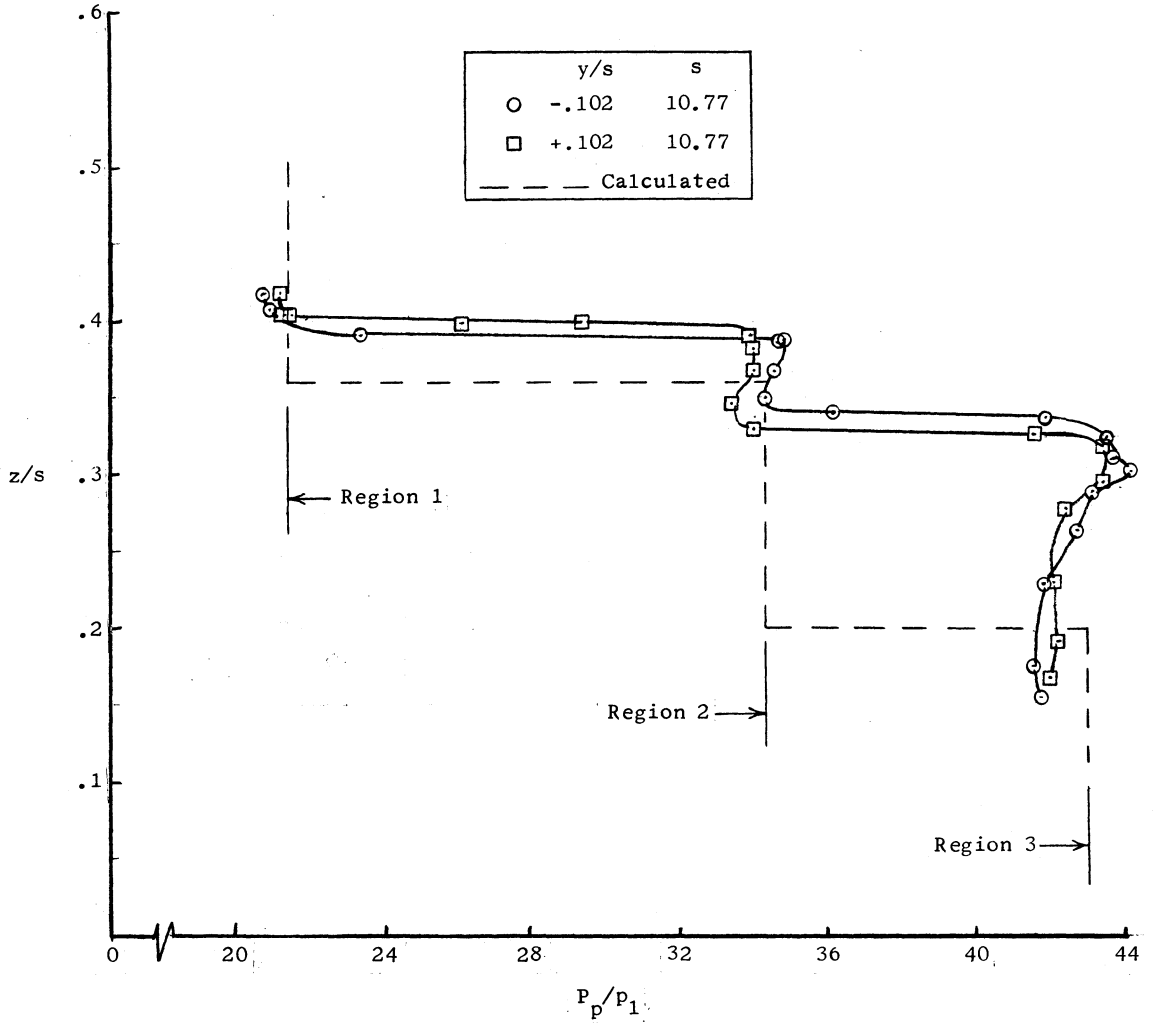

(d) $y/s = \pm 0.102$.

Figure 10.- Continued.

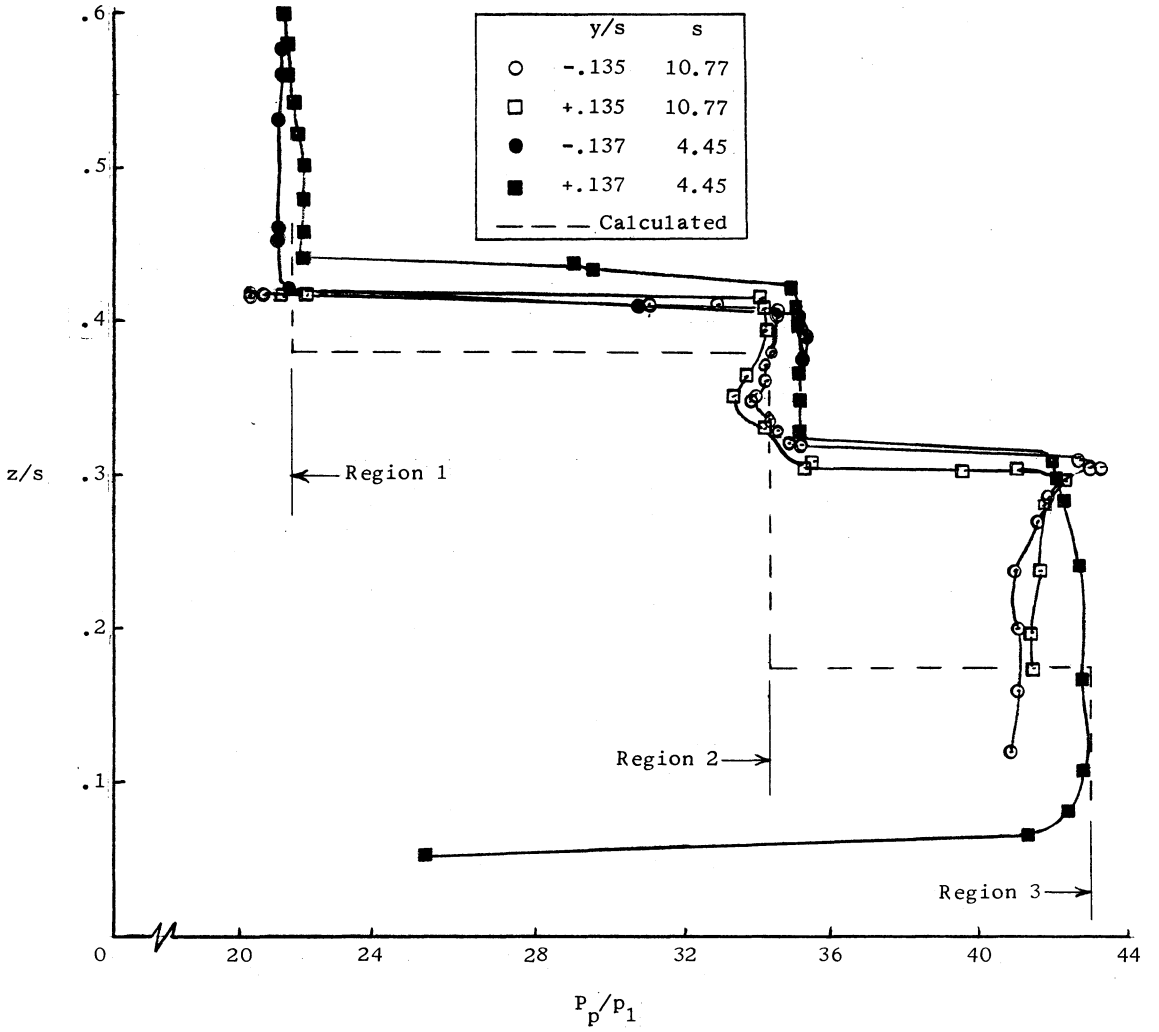

(e) y/s = ±0.136.

Figure 10.- Continued

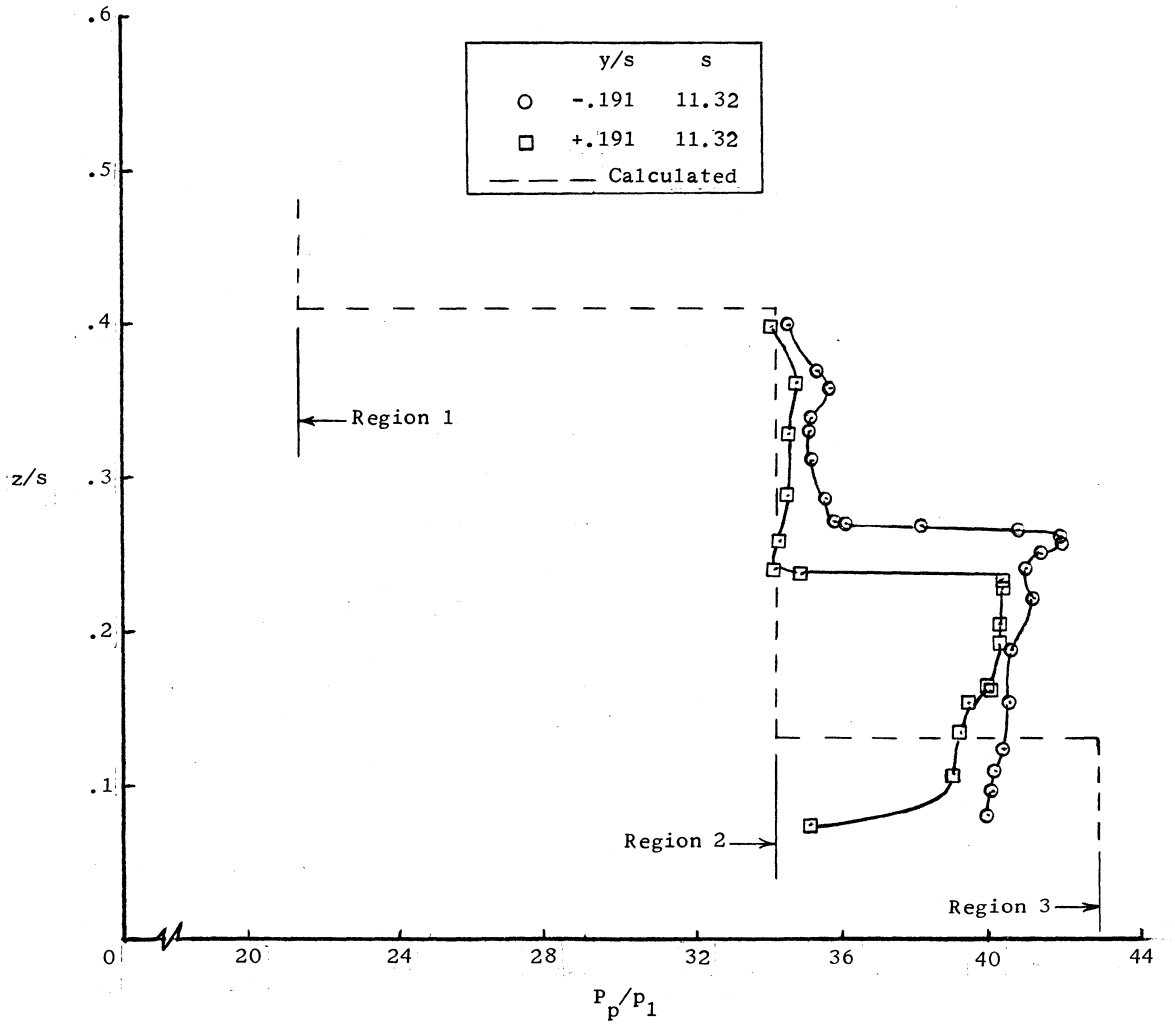

(f) $y/s = \pm 0.191$.

Figure 10.- Concluded.

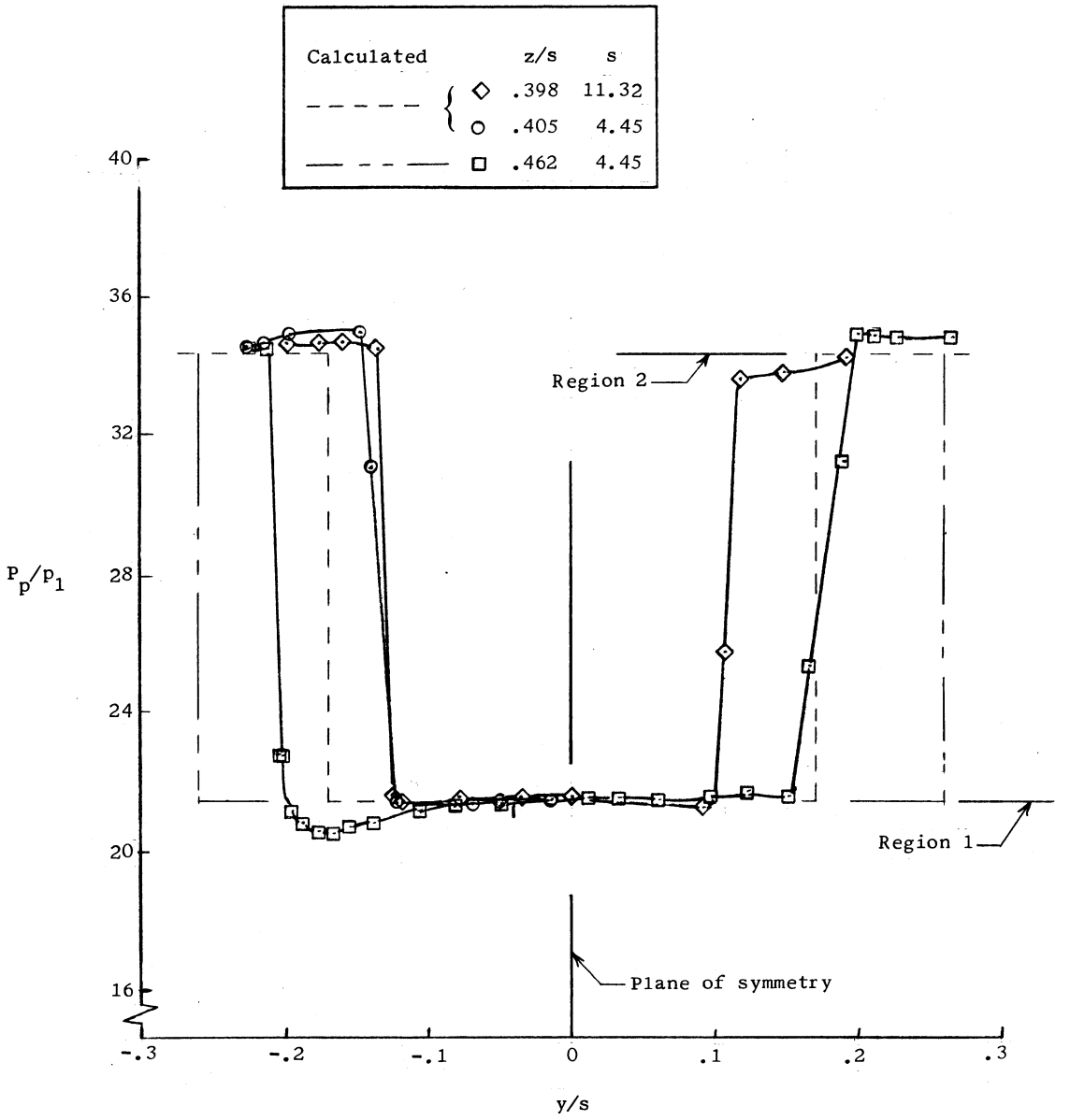

Figure 11.- Lateral pitot pressure survey.

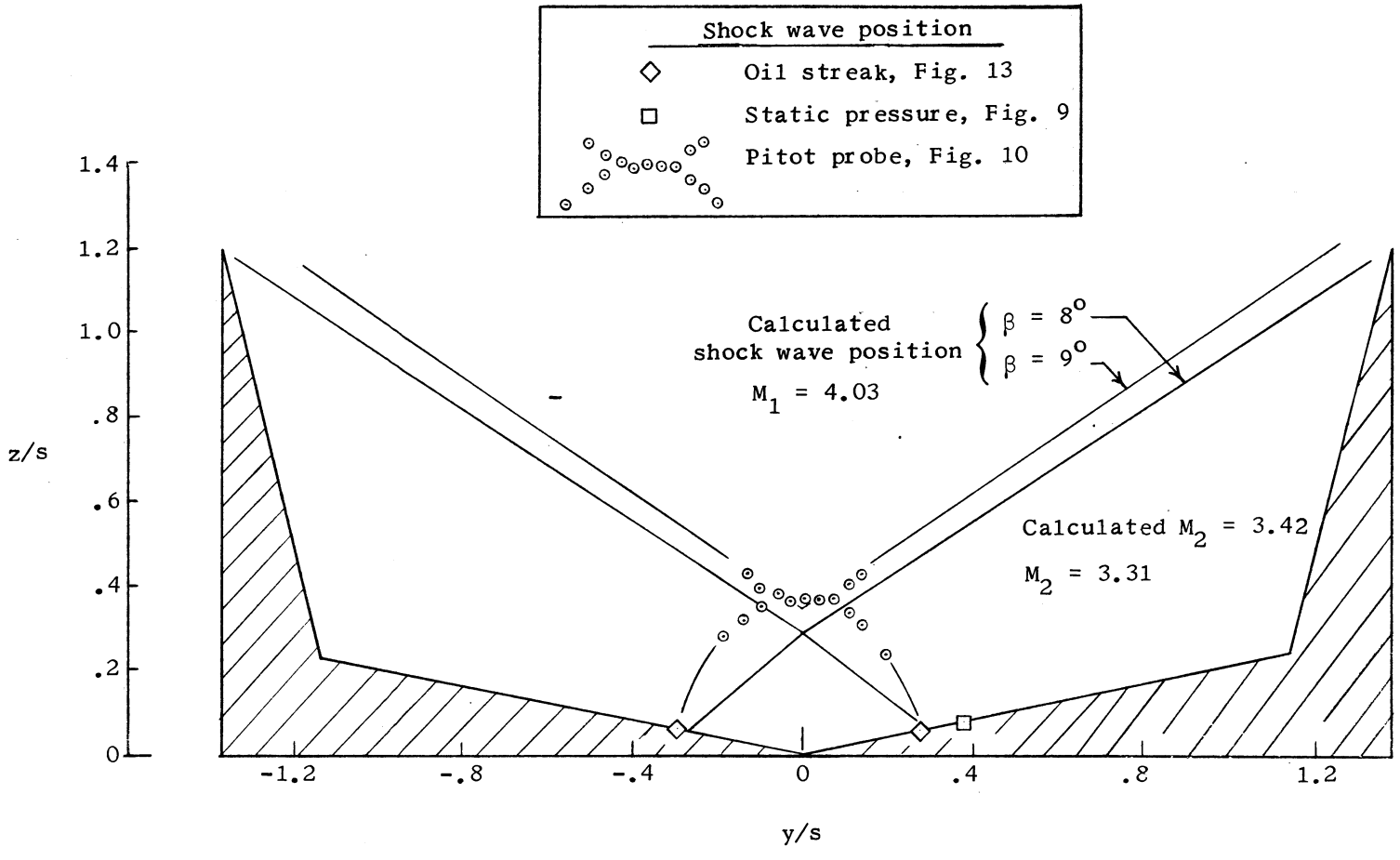

Figure 12.- Flow field at s = 1/2 L.

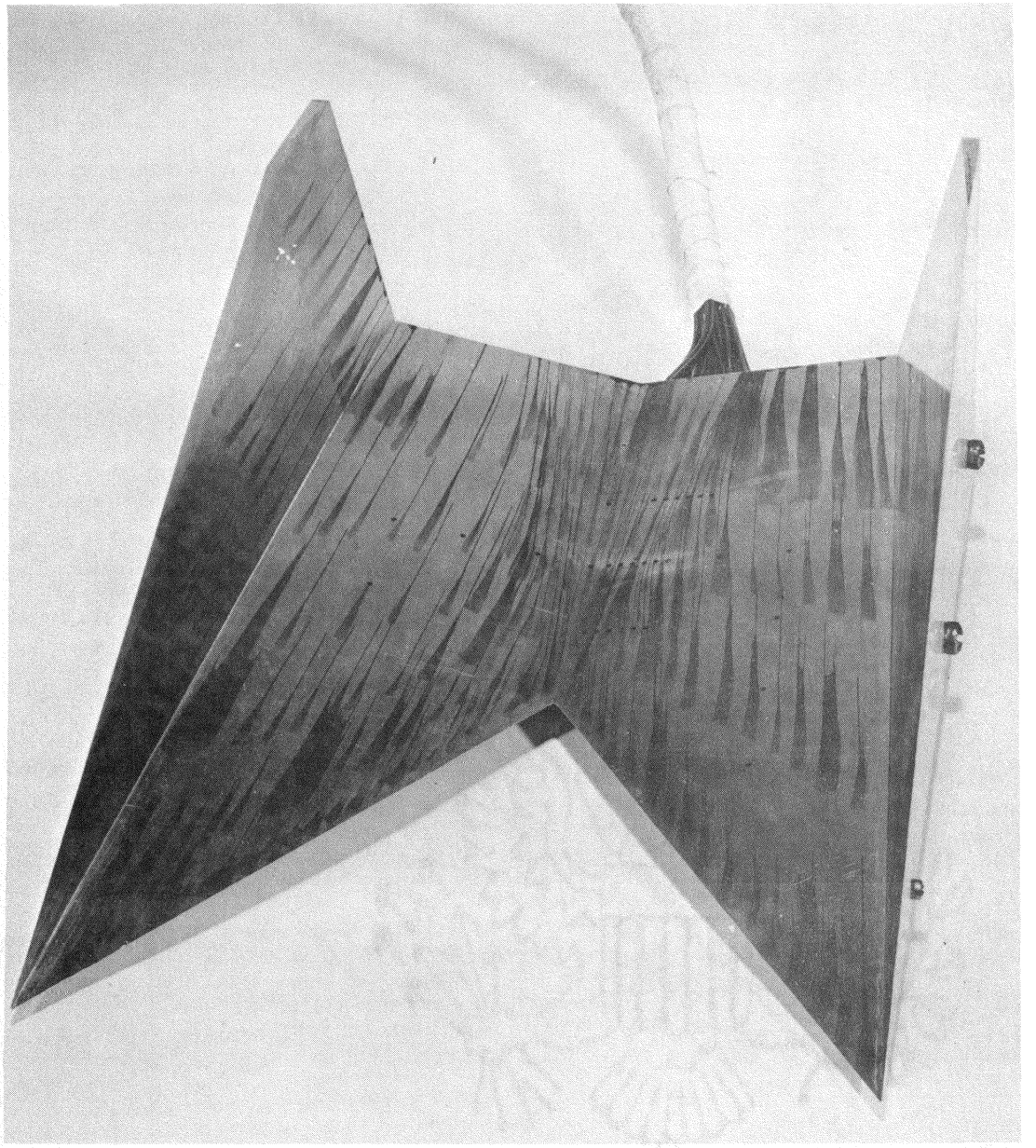

Figure 13.- Oil-streak photograph.

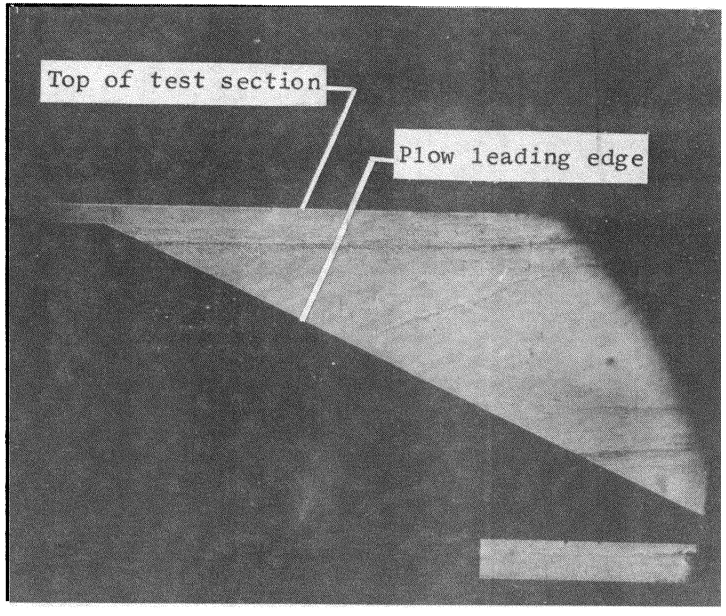

(a) $M_1 = 0.$

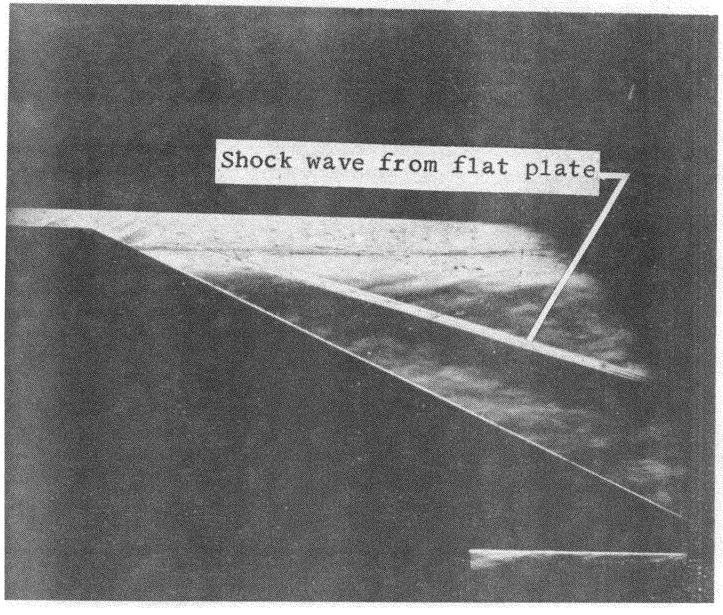

(b) $M_1 = 4.03.$

Figure 14.- Schlieren photograph.

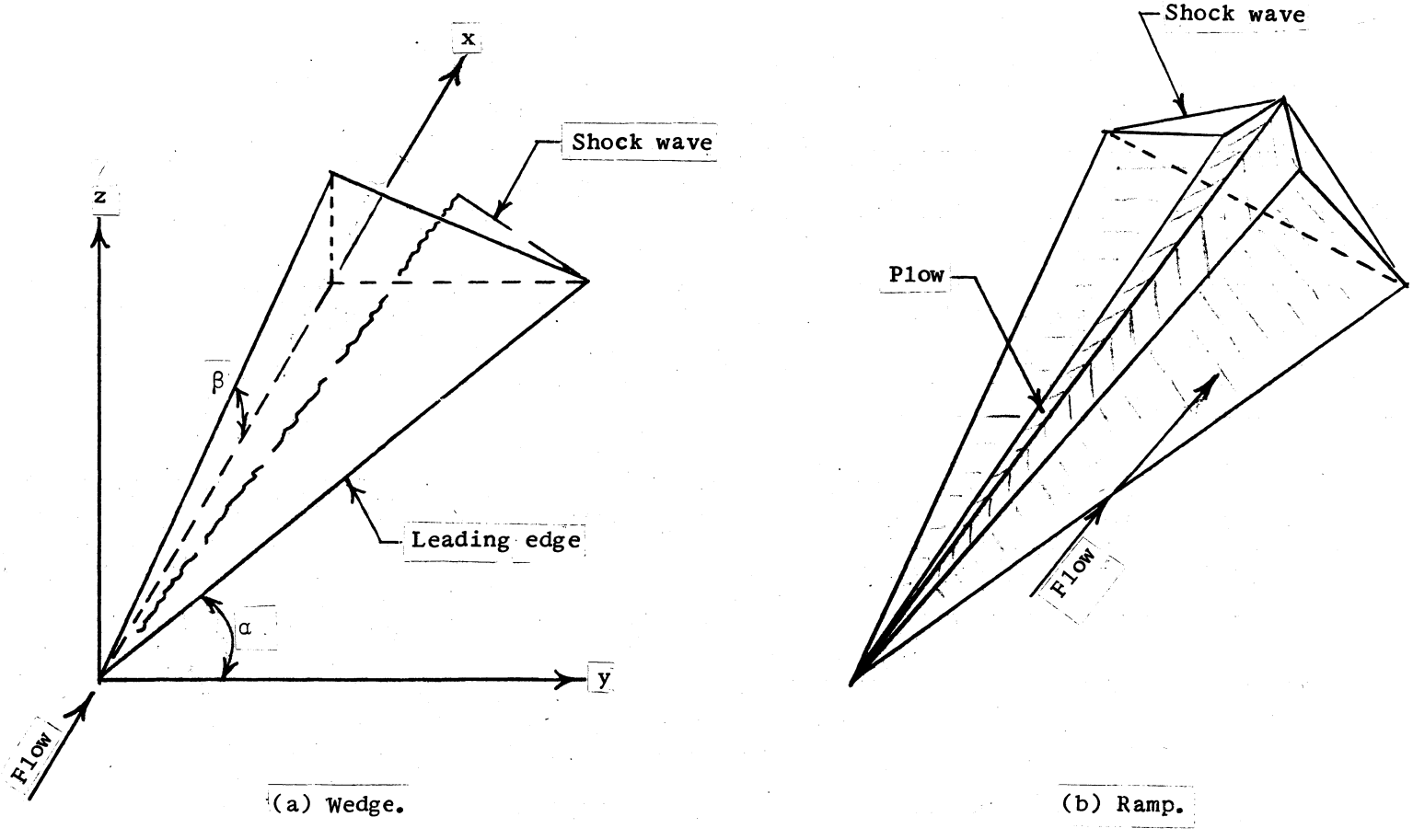

Figure 15.- Horizontal leading-edge configuration.

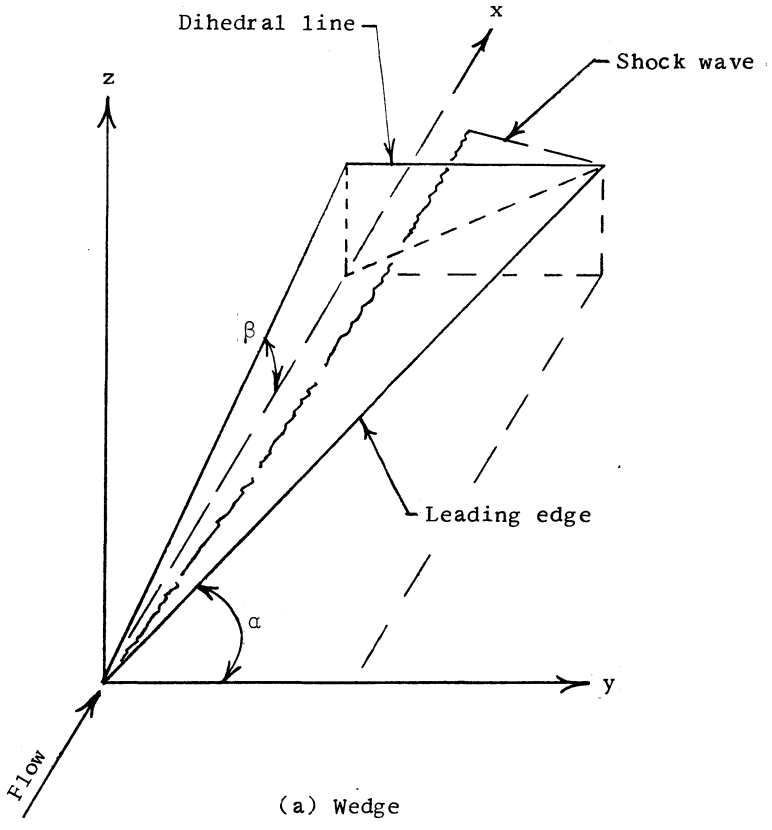

(a) Wedge

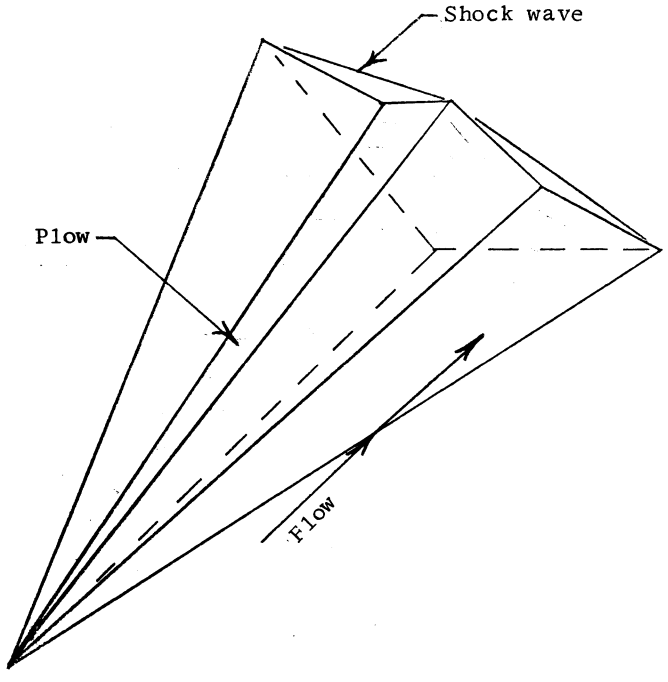

(b) Ramp

Figure 16.- Horizontal compression surface configuration.

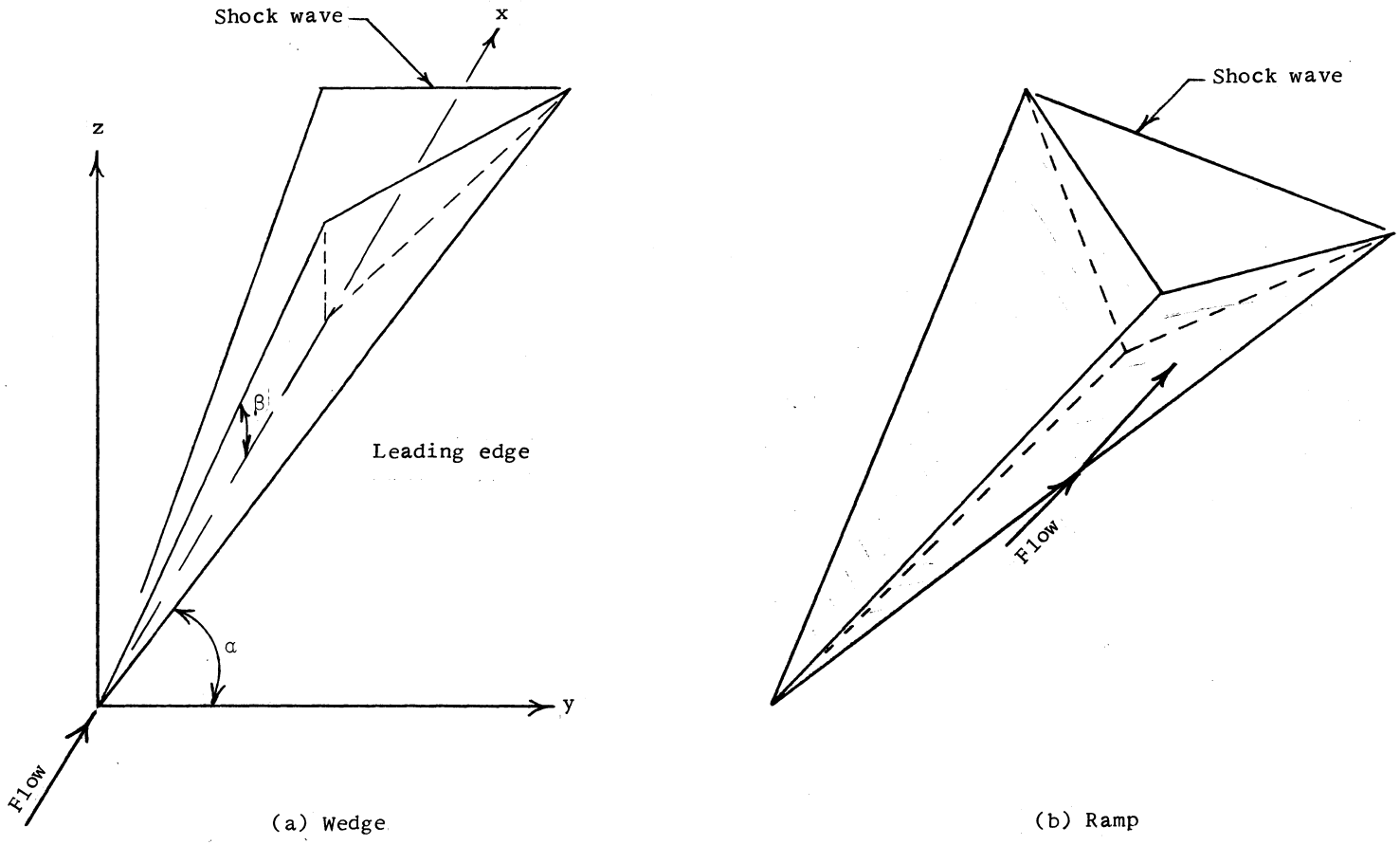

Figure 17.- Streamline-traced configuration.

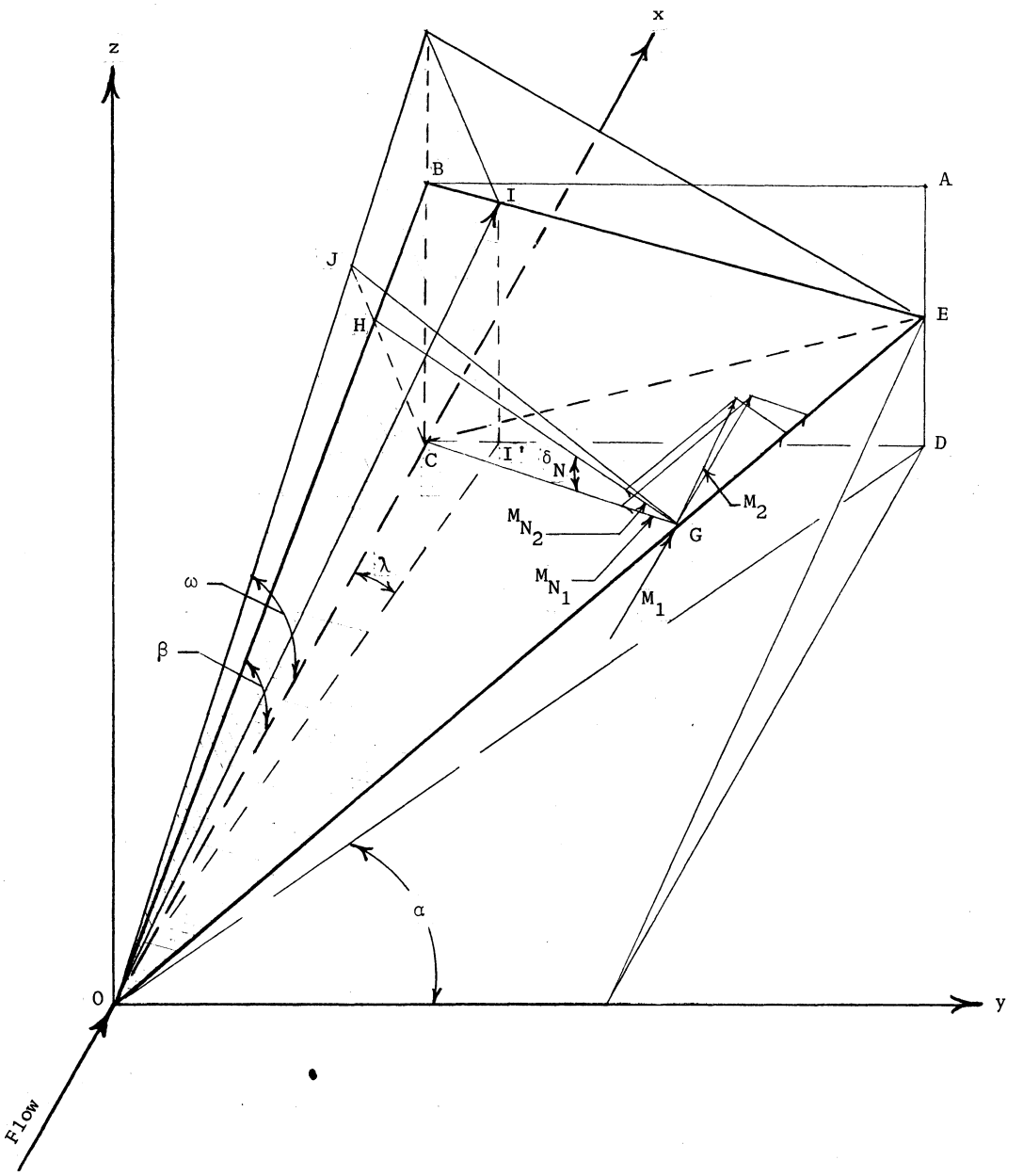

Figure 18.- Generalized mathematical model.

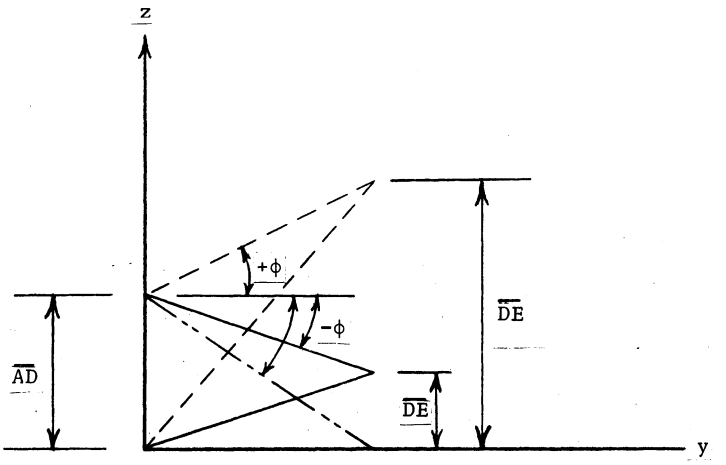

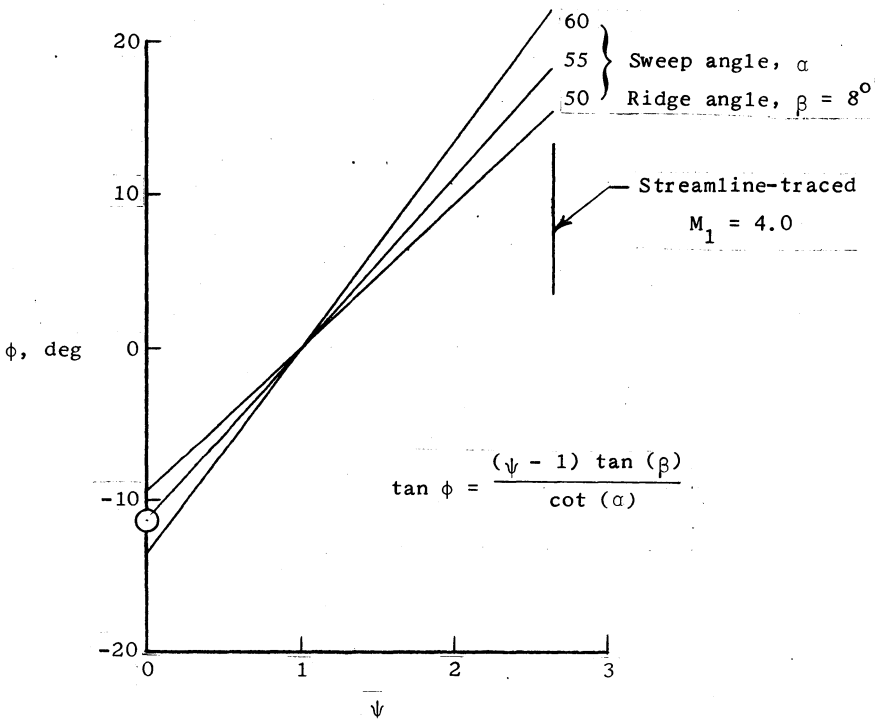

Figure 19.- Dihedral parameter.

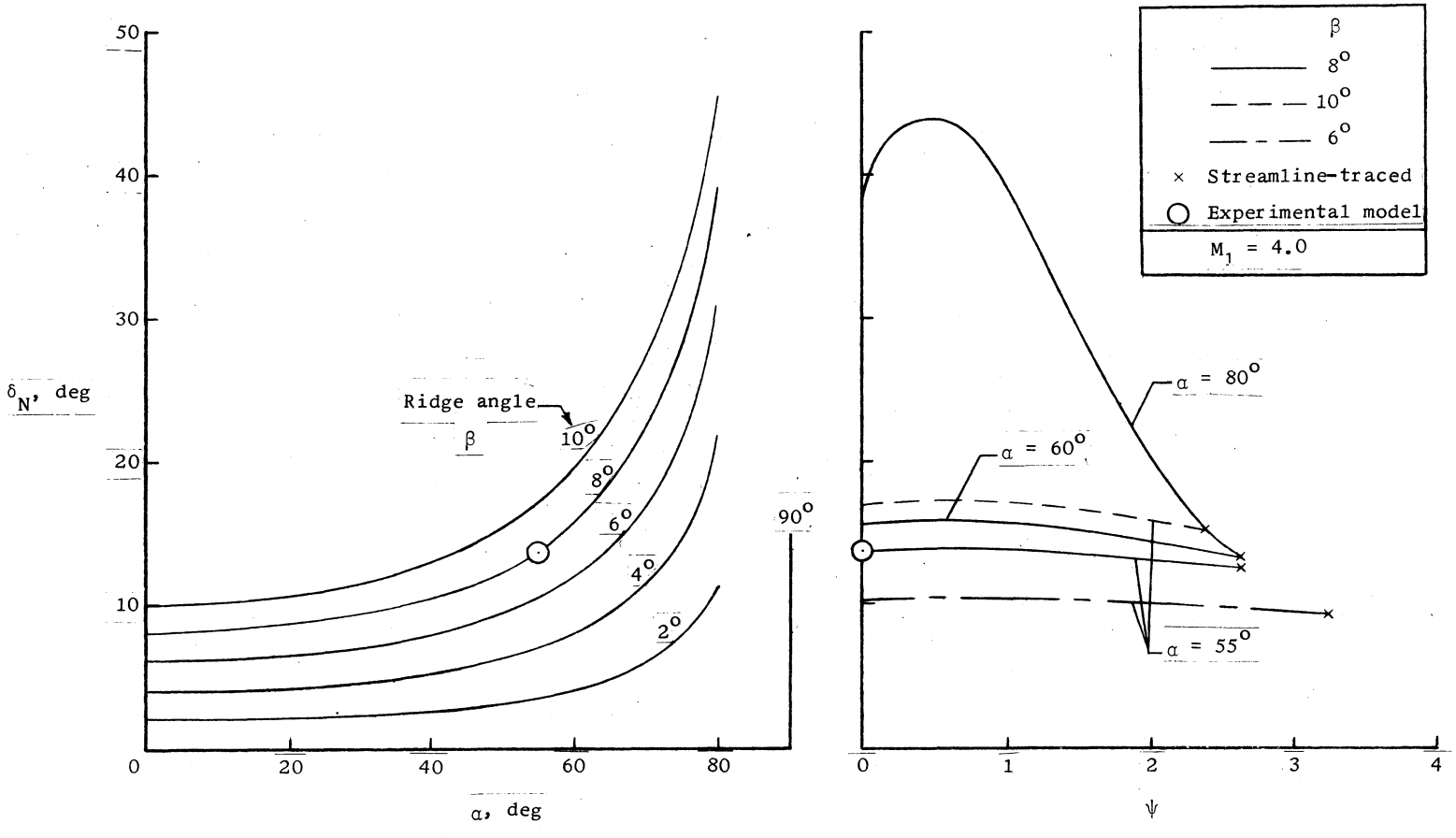

(a) Sweep angle (ψ = 0).

(b) Dihedral.

Figure 20.- Parametric effect of sweep and dihedral on flow deflection normal to leading edge.

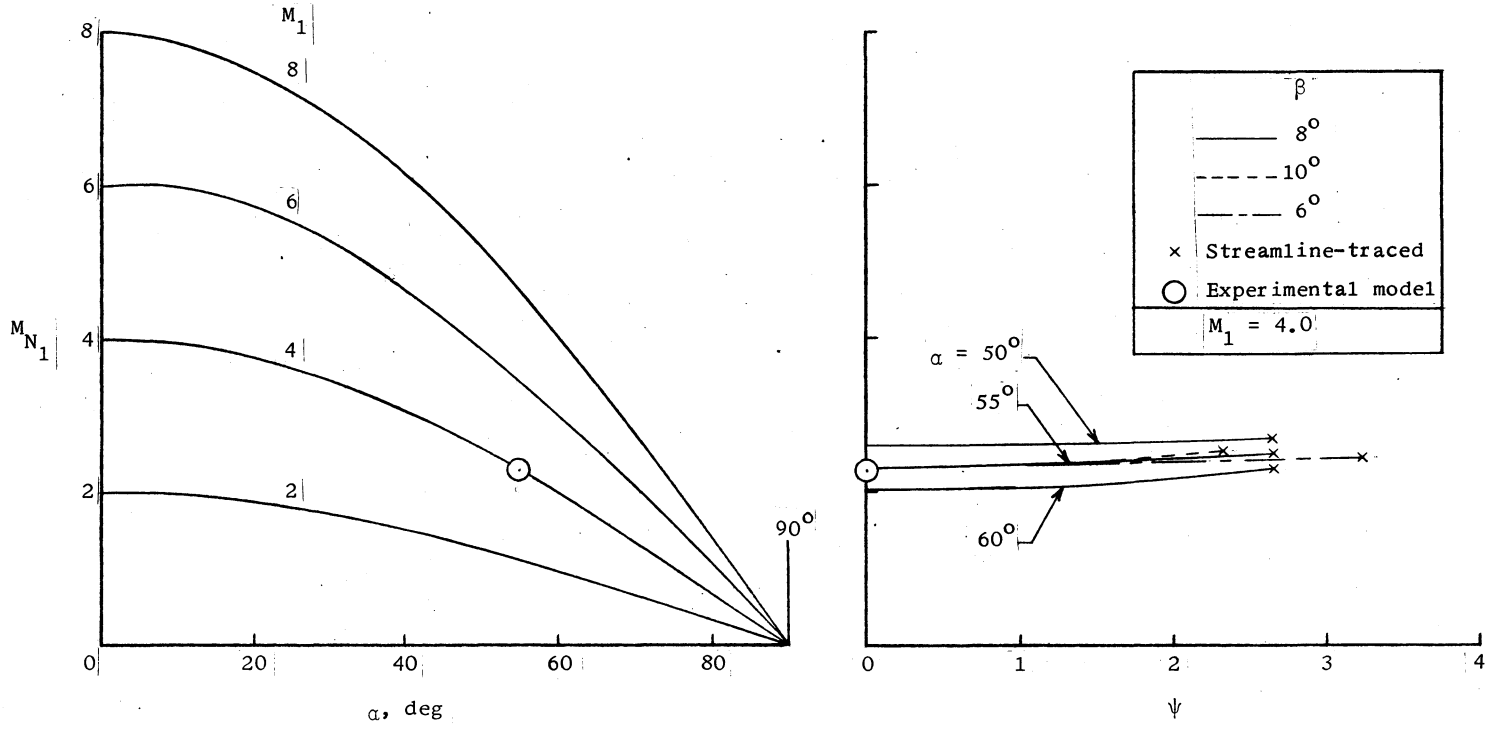

(a) Sweep angle (ψ = 0).

(b) Dihedral.

Figure 21.- Parametric effect of sweep and dihedral on free-stream Mach number normal to leading edge.

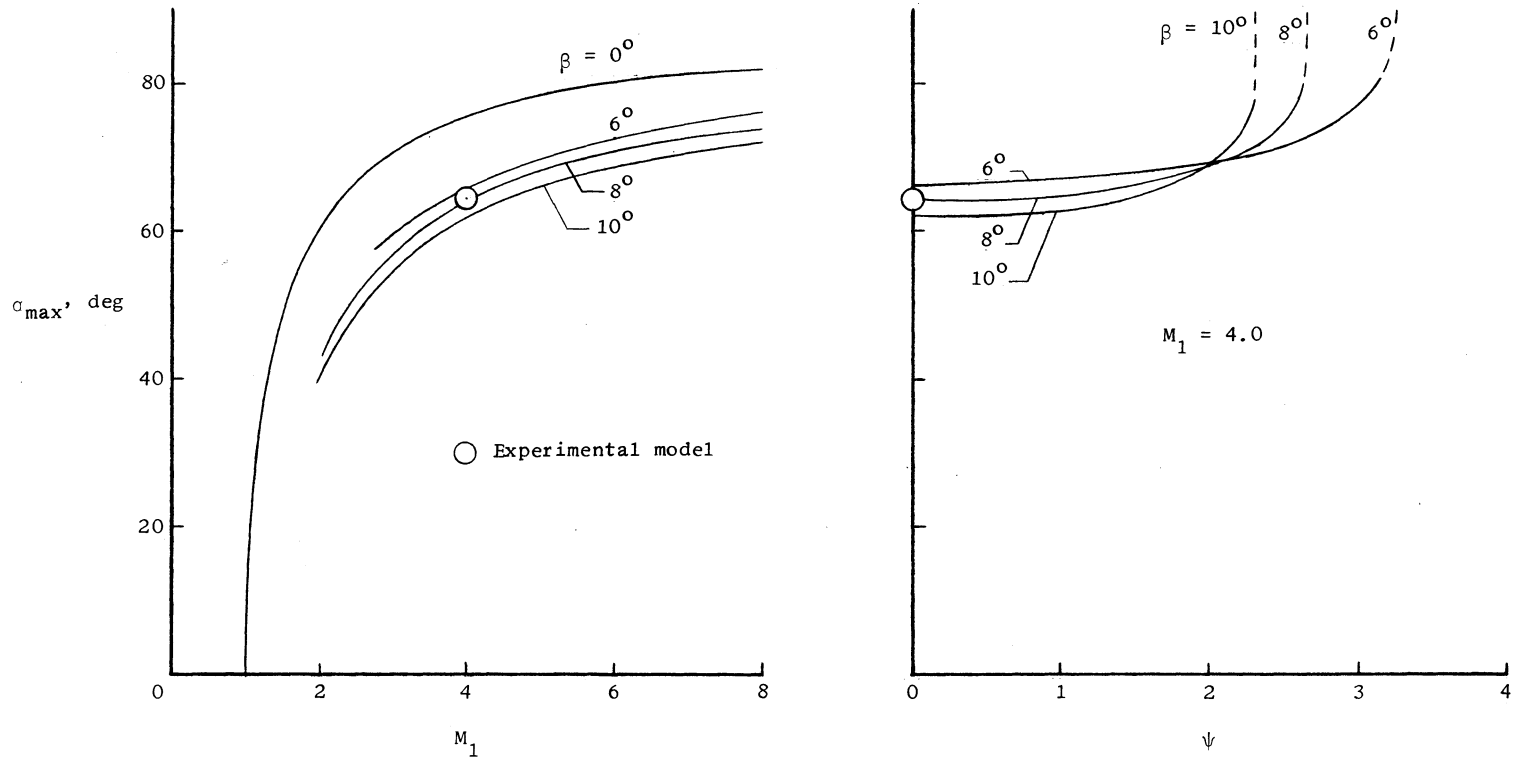

(a) Mach number (ψ = 0).

(b) Dihedral.

Figure 22.- Parametric effect of Mach number and dihedral on maximum sweep angle.

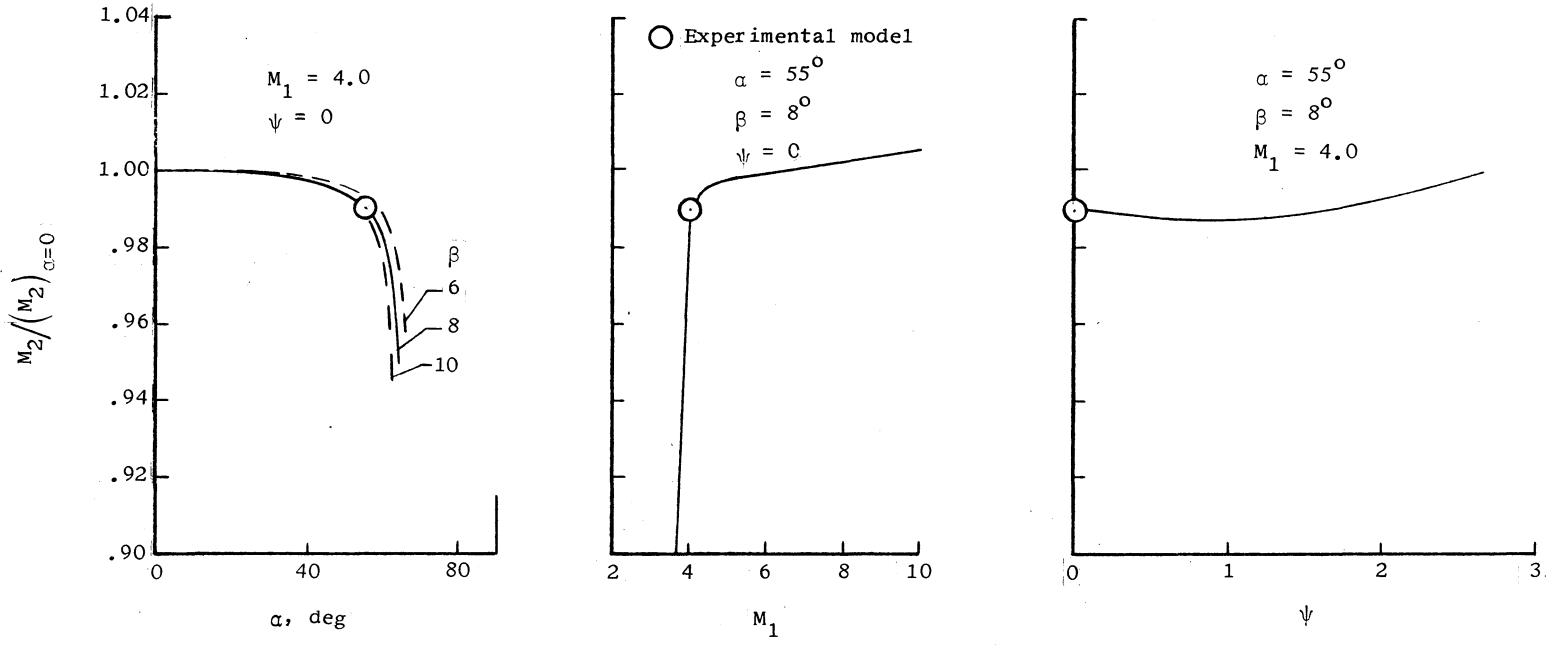

(a) Sweep angle.

(b) Mach number.

(c) Dihedral.

Figure 23.- Parametric effect of sweep, Mach number, and dihedral on M_2.

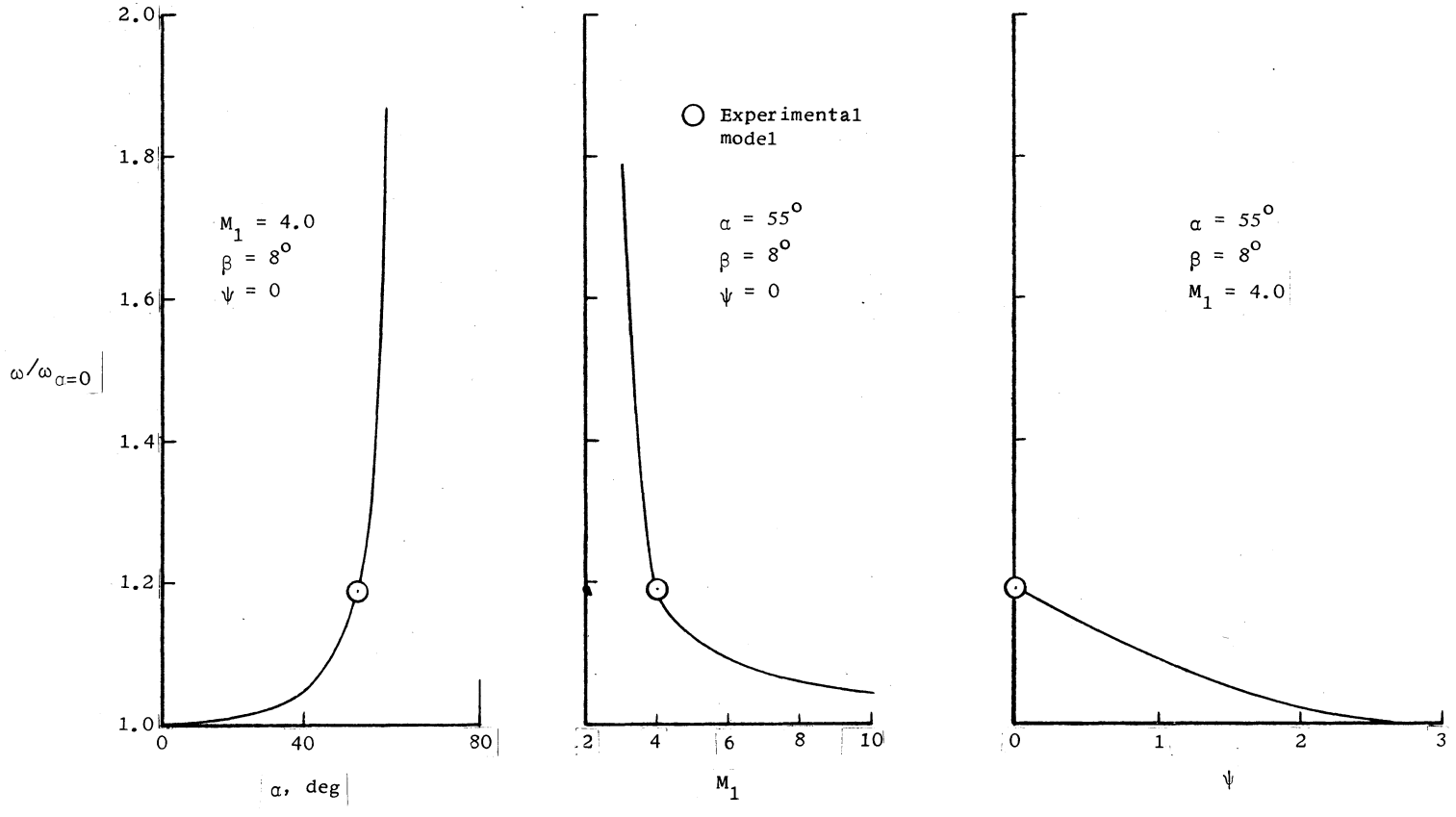

(a) Sweep angle. (b) Mach number. (c) Dihedral.

Figure 24.- Parametric effect of sweep, Mach number, and dihedral on shock wave position.

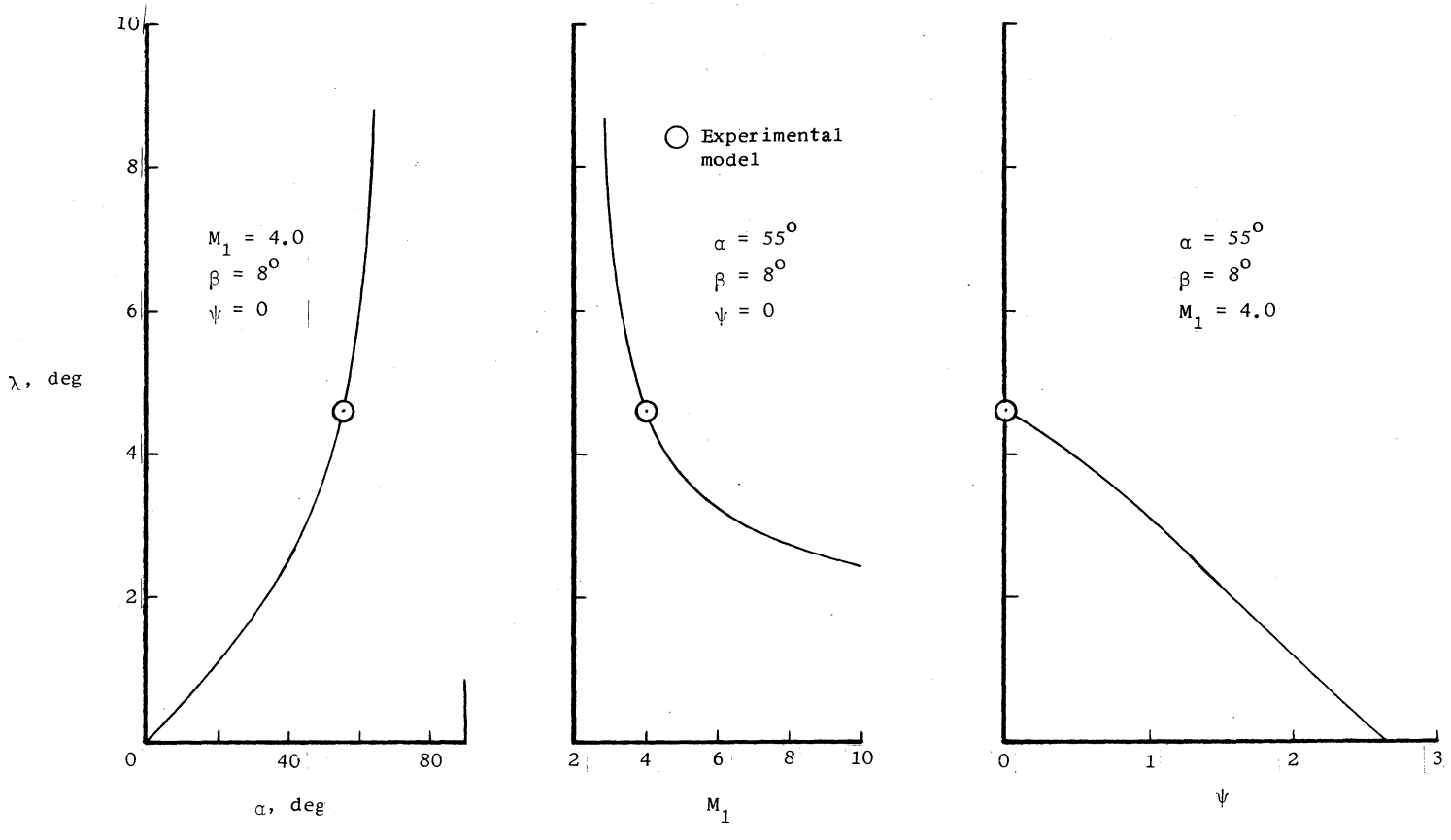

(a) Sweep angle. (b) Mach number. (c) Dihedral.

Figure 25.- Parametric effect of sweep, Mach number, and dihedral on cross flow.

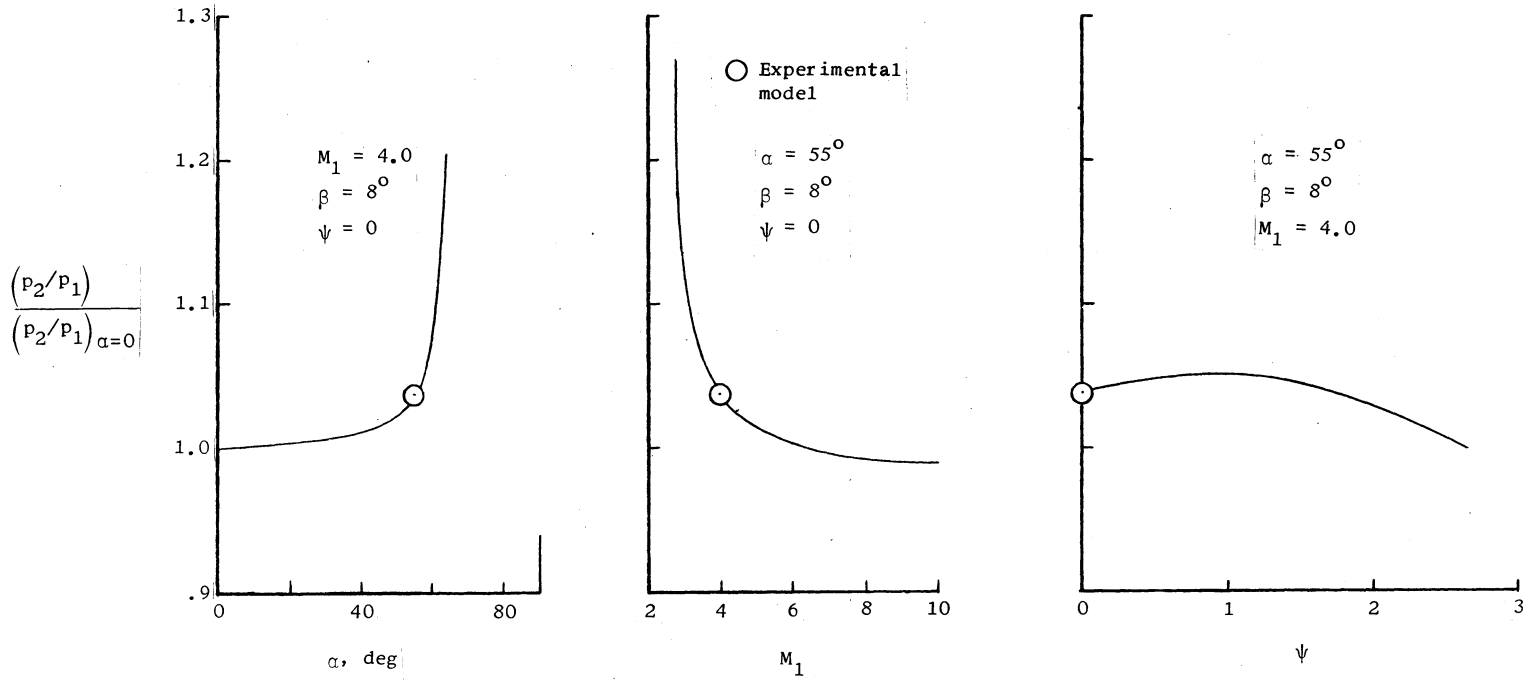

(a) Sweep angle.

(b) Mach number.

(c) Dihedral.

Figure 26.- Parametric effect of sweep, Mach number, and dihedral on static pressure.

AN EXPERIMENTAL INVESTIGATION OF THE FOREBODY OF A HYPERSONIC INLET MODEL AND A COMPARISON WITH THEORY

By

Carl Arthur Trexler

ABSTRACT

An experimental investigation of the flow field of a hypersonic inlet forebody model has been conducted in a Mach 4 airstream. Test section Reynolds number was approximately 6.6×10^7 per meter at a stagnation pressure of 13.6 atmospheres. The model consisted of two 8° wedges in the same plane and sloping toward each other, whose leading edges made angles of 55° to the approaching flow. The side walls were designed to follow the flow streamlines on the wedge surfaces and the shock waves from the wedge leading edges. The data was obtained from surface static pressure taps, pitot probe surveys, oil-streak tests, and schlieren photographs.

The results of the investigation indicate that the leading-edge shock waves join in a manner producing a region of three-dimensional, conical-like flow near the model's plane of symmetry. The flow and shock wave structure in this region were similar to the corner flow situation and the region size was underpredicted by the theoretical analysis. In the analysis the free-stream flow was broken into velocity components normal and tangential to the leading edge and utilized two-dimensional methods. It was possible to predict the flow properties and shock wave structure with confidence outside the center region,

although the experimental Mach number was approximately 4 percent less than the calculated value due to viscous effects on the model surface. An appendix is included which uses the analysis to make a parametric study of several swept wedge configurations.